Nitrogen-Substitution in the Flapping Wings of Cyclooctatetraene-Fused Molecules

Kensuke Suga,[1] Takuya Yamakado,[1] and Shohei Saito*[1]

[1]Graduate School of Science, Kyoto University, Kitashirakawa Oiwake, Sakyo, Kyoto 606-8502, Japan

E-mail: s_saito@kuchem.kyoto-u.ac.jp

Shohei Saito

Shohei Saito received his Ph.D. degree from Kyoto University in 2010.
After working as an Assistant Professor of Nagoya University, he has been an Associate Professor of Kyoto University since 2016. His research interest is focused on flapping molecules (FLAP) for photofunctional systems. He received The Asian and Oceanian Photochemistry Association (APA) award for young scientist 2018.

Abstract

New synthetic protocols to the nitrogen-embedded flapping molecules have been developed. Gram-scale synthesis of a key precursor, tetraamine of dibenzo[a,e]cyclooctatetraene has been established for designing flapping quinoxaline and flapping phenazineimide. The impact of the nitrogen substitution on the photophysical properties and the viscosity-probing function has been investigated in comparison with the reported flapping anthraceneimide.

Keywords: Excited-state planarization, Fluorescent molecule, Viscosity probe

1. Introduction

Flapping molecules (FLAP) with the formal 8π ring at its center have attracted attention as a versatile photofunctional system.[1] While dibenzo[b,f]oxepin[2] has been recognized as a classical fluorophore with the large Stokes shift that shows a bent-to-planar conformational change in the lowest singlet excited state (S_1), a variety of functions and applications of the FLAP series have been recently demonstrated, such as multi-color fluorescent dye,[3] highly sensitive viscosity probe,[4] ratiometric force probe (flexible mechanophore),[5] and light-melt adhesive.[6] The mechanism of the excited-state planarization has also been focused in relation to the excited-state aromaticity.[7] In this context, structural diversity of the conformationally flexible molecules has been rapidly enriched in recent studies, such as π-expanded cyclooctatetraene (COT),[3–6,8] dihydrophenazine,[9] phenothiazine,[10] dibenzoarsepin,[11] as well as π-expanded oxepin.[12] On the other hand, the effect of nitrogen substitution to the "wings" of the flapping molecules has not been studied, despite the efficacy of the nitrogen-doping has been widely recognized in tuning electronic structures and optical properties of polycyclic aromatic hydrocarbons (PAHs).[13] Here, we have developed new synthetic protocols to the nitrogen-embedded flapping molecules bearing quinoxaline and phenazineimide wings (Figure 1). Since the flapping phenazineimide shows an environment-sensitive fluorescence, its photophysical properties and viscosity-probing function have been investigated in comparison with the previously reported flapping anthraceneimide.
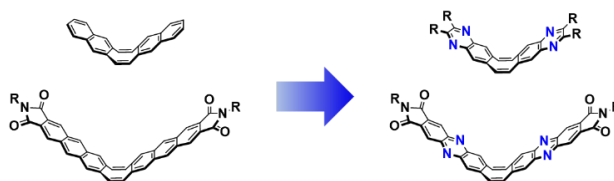

Figure 1. Nitrogen-substitution of the reported flapping naphthalene[14] and flapping anthraceneimide[3–5] (left), providing novel flapping quinoxaline and flapping phenazineimide (right).

2. Results and Discussion

To develop the synthetic route to the nitrogen-embedded flapping systems, a key precursor of dibenzo[a,e]cyclooctatetraene(COT)-2,3,8,9-tetraamine was prepared from the previously reported tetrabromo-substituted dibenzo[a,e]COT **1** (Figure 2).[4b] First, Pd-catalyzed imination of **1** with benzophenone imine provided **2** in 81% yield. The following hydrolysis of **2** in acidic conditions led to an immediate precipitation of the corresponding tetraamine **3** in a protonated form. Facile filtration process realized gram-scale synthesis of **3**. Since the non-protonated, neutralized form of **3** is highly electron-rich and thus gradually decomposed by spontaneous air oxidation, the protonated form of **3** was treated for the next reactions. Flapping quinoxaline **FLAP1** was prepared by condensation of **3** with 3,4-hexanedione in 68% yield. Next, we attempted to synthesize flapping phenazine **5** (Figure S2.1), but the coupling reaction[15] of **3** with 1,2-dibromo-4,5-dimethylbenzene as well as the reaction of **1** with 4,5-dimethylbenzene-1,2-diamine failed to give **5**, probably due to the poor solubility of products. To improve the solubility, we designed flapping phenazineimide **FLAP2** bearing bulky 2,6-diisopropylphenyl substituents at the terminal positions. Pd-catalyzed coupling reaction of **3** with dibromo-substituted phthalimide successfully provided **FLAP2** in 28% yield.
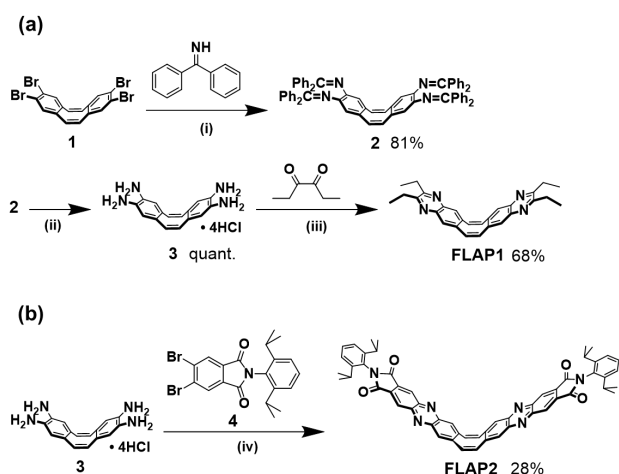
Figure 2. Synthesis of (a) **FLAP1** and (b) **FLAP2**. Reagents and conditions: (i) Ph₂C=NH, Pd₂(dba)₃, (±)-BINAP, NaO^{t}Bu, toluene, reflux, 42 h; (ii) HCl, H₂O/THF, 25 °C, 4.5 h; (iii) 3,4-hexanedione, CHCl₃/AcOH, 70 °C, 18 h; (iv) **4**, SPhos Pd G2, SPhos, Cs₂CO₃, toluene, reflux, 18 h.

Crystal structures of **FLAP1** and **FLAP2** were obtained with bent conformations (Figure 3). The COT bending angle, defined in Figure 5a, were 43.3° and 42.2° for **FLAP1**, and 40.3° for **FLAP2**. Bond lengths of the central COT moieties indicated that two π systems of the wings are not effectively conjugated due to the bent form of the COT ring, which is supported by the DFT calculations in the ground S_0 state (Figure S6.9, S6.11). Consistent with the needle-like crystal morphology, the V-shaped **FLAP1** molecules form a unique two-fold columnar π-stacking structure. The quinoxaline wings are tightly stacked on both sides, in which the interplanar distances are both 3.4 Å. In the block crystal of **FLAP2** recrystallized from a chlorobenzene/^{i}PrOH solution, the V-shaped molecules are not π-stacked in the columnar manner due to the terminal bulky groups. Instead, the phenazineimide moiety forms a cofacial packing only on one side with the 3.4-Å interplanar distance. The other side of the phenazineimide unit sandwiches a chlorobenzene molecule with two **FLAP2** molecules.
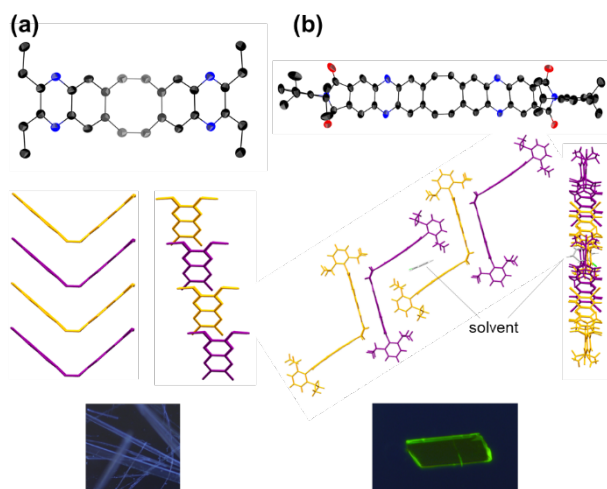

Figure 3. Single-crystal X-ray structure analysis (top) of (a) **FLAP1** and (b) **FLAP2** (50% probability for the thermal ellipsoids). Packing structures from different views are shown in the middle. Fluorescent images of each crystal under 365-nm UV light are displayed in the bottom.
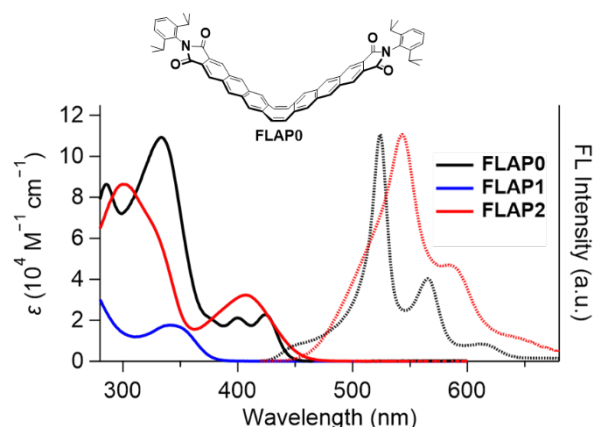

Figure 4. UV-visible absorption and fluorescence (FL) spectra of **FLAP0** (black line), **FLAP1** (blue line), and **FLAP2** (red line) in CHCl₃. Excitation wavelength: 340 nm for **FLAP1**, and 420 nm for **FLAP0** and **FLAP2**. The FL spectrum of **FLAP1** is not shown due to the very low FL quantum yield ($\Phi_F < 0.001$).

Although the **FLAP1** crystal showed a faint blue fluorescence (Figure 3a, bottom; see the FL spectrum in Figure S4.8), practically no emission was observed in solution. The lowest-energy absorption band does not reach the visible region (Figure 4, blue line). On the other hand, **FLAP2** has a visible absorption band at 408 nm, and a green fluorescence (FL) at 543 nm was observed in a CHCl₃ solution (Figure 4, red lines). Compared with **FLAP0**, the green FL band has a remarkable shoulder around the short-wavelength region (450–520 nm). The large Stokes shift of 6100 cm^{-1} suggested a bent-to-planar conformational change in S_1. FL quantum yield (Φ_F) and FL lifetime (τ_F) of **FLAP2** were determined to be 0.021 and 0.5 ns, respectively. These values are distinct from those of **FLAP0** (Φ_F = 0.31 and τ_F = 9.8 ns in CHCl₃). Lower Φ_F and shorter τ_F of **FLAP2** can be attributed to fast nonradiative decay, induced by the nitrogen substitution. Solvent dependence was negligible in absorption (Figure S4.2), while a slightly red-shifted fluorescence was observed in DMF (Figure S4.3).

To interpret the large Stokes shift based on the excited-state behavior, constrained TD-DFT calculations were conducted for the model structures, **FLAP0′** and **FLAP2′**, in which the terminal bulky substituents were replaced by hydrogen atoms for reducing the computational cost (Figure 5). Their S_1 energy profiles were delineated by plotting the total energies of the S_1 optimized geometries depending on the fixed COT bending angle. As a result, both S_1 profiles gave double-minimum potentials with the two minima at the bent and planar geometries.
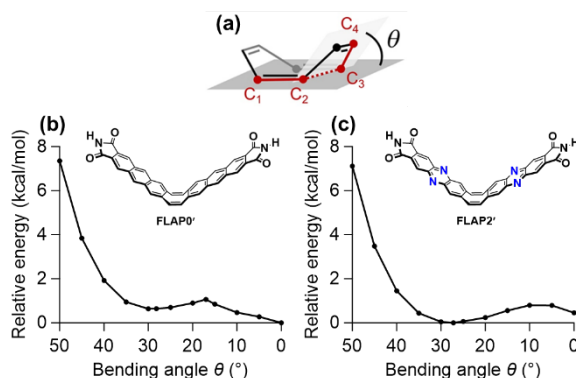

Figure 5. (a) Definition of the COT bending angle. Calculated S_1 energy profiles of (b) **FLAP0′** and (c) **FLAP2′** in C_{2v} symmetry. The constrained structural optimizations in S_1 were performed at the TD-PBE0/6-31+G(d) level of theory.

As for **FLAP0′**, we have previously reported[4a] that the small shoulder FL around 450 nm can be assigned as the emission from the S_1 local minimum, at which the anthraceneimide moiety is excited in the bent conformation, and that the intense FL at 520 nm with the large Stokes shift is emitted from the S_1 global minimum, at which the effectively π-conjugated system is formed in the planarized conformation. This explanation can be also applied to **FLAP2′**. In the S_1 profile of **FLAP2′** calculated at the TD-PBE0/6-31+G(d) level, the relative energy of the bent minimum is slightly lower than that of the planar S_1 minimum. This is consistent with the more remarkable shoulder FL (450–520 nm) of **FLAP2′** compared with that of **FLAP0′**. The detailed calculation results are displayed in the Supporting Information, in which the S_1 configuration switch during the bent-to-planar conformational change as well as the energetically close S_1 configurations at different planar geometries are discussed.
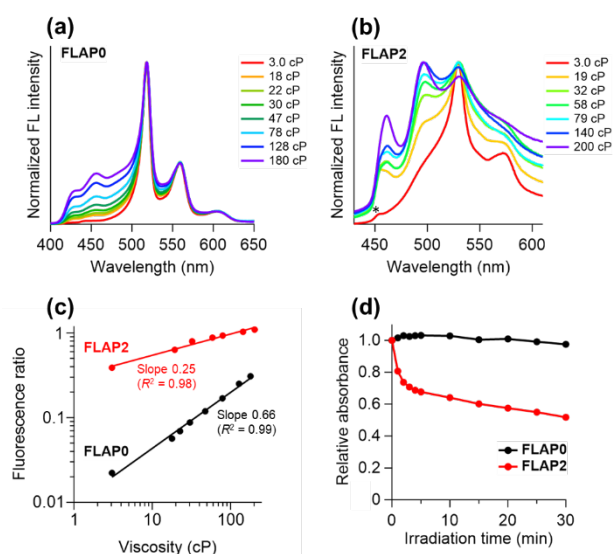

Figure 6. Viscochromism of (a) **FLAP0** and (b) **FLAP2** in a mixed solvent system of hexadecane/mineral oil. Excitation wavelength: 350 nm for **FLAP0** and 400 nm for **FLAP2**. A small band with asterisk (*) was assigned as a Raman peak of the solvent. (c) Förster–Hoffmann plot. The FL ratio values in Figure 6a (I_{460}/I_{518} for **FLAP0**, black) and Figure 6b (I_{497}/I_{530} for **FLAP2**, red) were plotted against the bulk viscosity in the log–log graph. (d) Photodegradation behavior monitored at the 400-nm absorbance (in toluene, concentration: *ca.* 10^{-5} M). Continuous UV irradiation was conducted at 365 nm with 100 mW cm^{-2} intensity.

To endorse the dynamic conformational change in S_1, we performed the fluorescence measurements of **FLAP2** in viscous media. Since the spectral broadening was observed in DMSO/glycerol mixtures (Figure S4.6), we selected the nonpolar mixed solvent system of hexadecane/mineral oil for evaluating the viscosity dependence (Figure 6a-c). Bulk viscosity of the mineral oil itself was determined by a rotational viscometer to be 507 cP at 25 °C, and the Newtonian behavior was confirmed for the mixed solvent system. Namely, the bulk viscosity was constant regardless of the rotation speed of the spindle. As a result, both **FLAP0** and **FLAP2** showed viscosity-dependent dual FL properties. With the higher viscosity, the shoulder FL band around 450-500 nm became increased, indicating partially suppressed bent-to-planar conformational change in S_1. According to the Förster-Hoffmann plot, the spectral sensitivity to the viscosity change in the 3–200 cP range is relatively higher in **FLAP0**. In addition, it is worth noting that the photostability of **FLAP2** under UV irradiation is much weaker than that of **FLAP0** (Figure 6d and S4.5). To elucidate the photodegradation mechanism, we are currently collaborating with laser physicists.

3. Conclusion

Nitrogen substitution in the naphthalene and anthraceneimide wings of the photofunctional flapping molecules has been achieved. A key precursor of dibenzo[*a,e*]COT tetraamine was synthesized in gram scale. Coupling reactions with 1,2-diketone and with dibromo-substituted phthalimide afforded COT-fused quinoxaline dimer and phenazineimide dimer, respectively, as novel nitrogen-embedded flapping systems. While the V-shaped quinoxaline dimer formed a two-fold columnar π-stacking structure in the crystalline state, the flapping phenazineimide displayed viscosity-dependent dual fluorescence properties. Compared with flapping anthraceneimide, the effect of the nitrogen substitution on the photophysical properties was studied by experiments and theory. Since the phenazine unit plays versatile roles, such as boron-coordinating system,[16] metal ligands for coordination polymer,[17] ESIPT (excited-state intramolecular proton transfer) acceptors,[18] and redox active units showing PCET (proton coupled electron transfer),[19] the nitrogen-embedded flapping molecules have the potential to endow these roles with dynamic functions. In addition, similar heteroatom-substitution approach will further expand the flapping molecular series, leading to exploration of new functional systems.

References

1. S. Saito, *Molecular Technology: Materials Innovation, Vol. 3* (Eds.: H. Yamamoto, T. Kato), Wiley-VCH, Weinheim, **2019**, pp.17–51.
2. D. Shukla, P. Wan, *J. Am. Chem. Soc.* **1993**, *115*, 2990.
3. (a) C. Yuan, S. Saito, C. Camacho, S. Irie, I. Hisaki, S. Yamaguchi, *J. Am. Chem. Soc.* **2013**, *135*, 8842. (b) C. Yuan, S. Saito, C. Camacho, T. Kowalczyk, S. Irle, S. Yamaguchi, *Chem. Eur. J.* **2014**, *20*, 2193.
4. (a) R. Kotani, H. Sotome, H. Okajima, S. Yokoyama, Y. Nakaike, A. Kashiwagi, C. Mori, Y. Nakada, S. Yamaguchi, A. Osuka, A. Sakamoto, H. Miyasaka, S. Saito, *J. Mater. Chem. C* **2017**, *5*, 5248. (b) R. Kimura, H. Kuramochi, P. Liu, T. Yamakado, A. Osuka, T. Tahara, S. Saito, *Angew. Chem. Int. Ed.* **2020**, *59*, 16430. (c) R. Kimura, H. Kitakado, A. Osuka, S. Saito, *Bull. Chem. Soc. Jpn.* **2020**, *93*, 1102.
5. (a) R. Kotani, S. Yokoyama, S. Nobususe, S. Yamaguchi, A. Osuka, H. Yabu, S. Saito, **2020** *arXiv:2011.00202v2*. (b) T. Yamakado, K. Otsubo, A. Osuka, S. Saito, *J. Am. Chem. Soc.* **2018**, *140*, 6245.
6. S. Saito, S. Nobusue, E. Tsuzaka, C. Yuan, C. Mori, M. Hara, T. Seki, C. Camacho, S. Irle, S. Yamaguchi, *Nature Commun.* **2016**, *7*, 12094.
7. (a) R. Ayub, O. E. Bakouri, K. Jorner, M. Solà, H. Ottosson, *J. Org. Chem.* **2017**, *82*, 6327. (b) J. Toldo, O. E. Bakouri,

M. Solà, P.-O. Norrby, H. Ottosson, *ChemPlusChem* **2019**, *84*, 712. (c) M. Rosenberg, C. Dahlstrand, K. Kilså, Henrik Ottosson, *Chem. Rev.* **2014**, *114*, 5379−5425.

8. (a) T. Yamakado, S. Takahashi, K. Watanabe, Y. Matsumoto, A. Osuka, S. Saito, *Angew. Chem. Int. Ed.* **2018**, *57*, 5438. (b) M. Hada, S. Saito, S. Tanaka, R. Sato, M. Yoshimura, K. Mouri, K. Matsuo, S. Yamaguchi, M. Hara, Y. Hayashi, F. Röhricht, R. Herges, Y. Shigeta, K. Onda, J. D. Miller, *J. Am. Chem. Soc.* **2017**, *139*, 15792. (c) M. Ueda, K. Jorner, Y. M. Sung, T. Mori, Q. Xiao, D. Kim, H. Ottosson, T. Aida, Y. Itoh, *Nature Commun.* **2017**, *8*, 346.

9. (a) Z. Zhang, W. Song, J. Su, H. Tian, *Adv. Funct. Mater.* **2019**, *30*, 1902803. (b) W. Chen, C.-L. Chen, Z. Zhang, Y.-A. Chen, W.-C. Chao, J. Su, H. Tian, P.-T. Chou, *J. Am. Chem. Soc.* **2015**, *137*, 8509. (c) Z. Zhang, Y.-S. Wu, K.-C. Tang, C.-L. Chen, J.-W. Ho, J. Su, H. Tian, P.-T. Chou *J. Am. Chem. Soc.* **2015**, *137*, 8509. (d) G. B. Schuster, S. P. Schmidt, B. G. Dixon, *J. Phys. Chem.* **1980**, *84*, 1841.

10. D.-G. Chen, Y. Chen, C.-H. Wu, Y.-A. Chen, M.-C. Chen, J.-A. Lin, C.-Y. Huang, J. Su, H. Tian, P.-T. Chou, *Angew. Chem., Int. Ed.* **2019**, *58*, 13297.

11. (a) I. Kawashima, H. Imoto, M. Ishida, H. Furuta, S. Yamamoto, M. Mitsuishi, S. Tanaka, T. Fujii, K. Naka, *Angew. Chem. Int. Ed.* **2019**, *58*, 11686. (b) P. B. Karadakov, S. Saito, *Angew. Chem. Int. Ed.* **2020**, *59*, 9228.

12. R. Kotani, L. Liu, P. Kumar, H. Kuramochi, T. Tahara, P. Liu, A. Osuka, P. B. Karadakov, S. Saito, *J. Am. Chem. Soc.* **2020**, *142*, 14985.

13. (a) A. L. Appleton, S. M. Brombosz, S. Barlow, J. S. Sears, J.-L. Bredas, S. R. Marder, U. H. F. Bunz, *Nat. Commun.* **2010**, *1*, 91. (b) M. Takase, T. Narita, W. Fujita, M. S. Asano, T. Nishinaga, H. Benten, K. Yoza, K. Müllen, *J. Am. Chem. Soc.* **2013**, *135*, 8031. (c) B. D. Lindner, Y. Zhang, S. Höfle, N. Berger, C. Teusch, M. Jesper, K. I. Hardcastle, X. Qian, U. Lemmer, A. Colsmann, U. H. F. Bunz, M. Hamburger, *J. Mater. Chem. C* **2013**, *1*, 5718. (d) Y. Tokimaru, S. Itoh, K. Nozaki, *Angew. Chem., Int. Ed.* **2015**, *54*, 7256. (e) H. Yokoi, Y. Hiraoka, S. Hiroto, D. Sakamaki, S. Shu, H. Shinokubo, *Nat. Commun.* **2015**, *6*, 8215. (e) Z. Zhang, Q. Zhang, *Mater. Chem. Front.* **2020**, *4*, 3419.

14. P. A. Wender, A. B. Lesser, L. E. Sirois, *Angew. Chem. Int. Ed.* **2012**, *51*, 2736.

15. J. K. Laha, K. S. S. Tummalapalli, A. Gupta, *Eur. J. Org. Chem.* **2013**, 8330.

16. Y. Min, C. Dou, H. Tian, Y. Geng, J. Liu, L. Wang, *Angew. Chem. Int. Ed.* **2018**, *57*, 2000.

17. M. Munakata, S. Kitagawa, N. Ujimaru, M. Nakamura, M. Maekawa, H. Matsuda, *Inorg. Chem.* **1993**, *32*, 826.

18. J. Piechowska, K. Virkki, B. Sadowski, H. Lemmetyinen, N. V. Tkachenko, D. T. Gryko, *J. Phys. Chem. A* **2014**, *118*, 144.

19. (a) H. Xie, Y. Wu, T. Liu, F. Wang, B. Chen, B. Liang, *Applied Energy*, **2020**, *259*, 114119. (b) M. N. Jackson, M. L. Pegis, Y. Surendranath, *ACS Cent. Sci.* **2019**, *5*, 831.

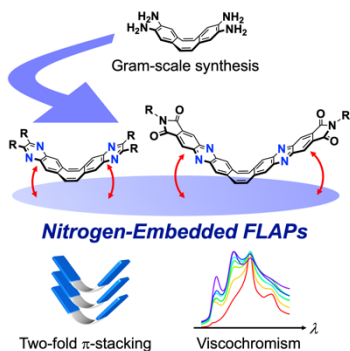**Graphical Abstract**

Nitrogen-Substitution in the Flapping Wings of Cyclooctatetraene-Fused Molecules

Kensuke Suga, Takuya Yamakado, and Shohei Saito*

<Summary>
Nitrogen atoms are embedded in the acene wings of the flapping molecules bearing a cyclooctatetraene ring at its center, and the nitrogen substitution effects are studied. V-shaped flapping quinoxaline molecules formed a columnar π-stacking structure in the crystalline phase. Flapping phenazineimide showed a viscosity-dependent dual fluorescence, originating from the double-minimum energy potential in the lowest singlet excited state.

<Diagram>

Gram-scale synthesis

Nitrogen-Embedded FLAPs

Two-fold π-stacking   Viscochromism

<p style="text-align: center;">Supporting Information</p>

Nitrogen-Substitution in the Flapping Wings of Cyclooctatetraene-Fused Molecules

Kensuke Suga,[1] Takuya Yamakado,[1] and Shohei Saito[*1]

[1]Graduate School of Science, Kyoto University, Kitashirakawa Oiwake-cho, Sakyo-ku, Kyoto 606-8502 (Japan)

Corresponding Author

s_saito@kuchem.kyoto-u.ac.jp

Contents

1. General information

Synthesis

All reagents and solvents were of commercial grade and were used without further purification unless otherwise noted. Tetrahydrofuran (THF) and dioxane were dried using Glass Contour solvent purification system. Thin layer chromatography (TLC) was carried out on aluminum sheets coated with silica gel 60 F_{254} (Merck). Column chromatography was performed on Wakogel® C-300 and C-400. ^{1}H and ^{13}C NMR spectra were recorded on a JEOL ECA-600 (600 MHz for ^{1}H and 151 MHz for ^{13}C) spectrometer. Chemical shifts were reported in ppm relative to the residual solvents as internal standards (CHCl$_3$: δ = 7.26 ppm for ^{1}H and δ = 77.16 ppm for ^{13}C; DMSO: δ = 2.50 ppm for ^{1}H and δ = 39.52 ppm for ^{13}C). High-resolution atmospheric-pressure-chemical-ionization time-of-flight mass spectrometry (HR-APCI-TOF-MS) was performed with a BRUKER micrOTOF model. Compounds **1**[S1] and **4**[S2], and **FLAP0**[S3] were synthesized according to the reported methods.

Photophysical measurements

UV-visible absorption spectra were recorded on a Shimadzu UV-3600 spectrometer. Steady-state fluorescence and excitation spectra were recorded on a JASCO FP-8500 spectrofluorometer. Absolute fluorescence quantum yields were determined on a HAMAMATSU C9920-02S apparatus. Fluorescence lifetimes were measured on a compact fluorescence lifetime spectrometer Hamamatsu Photonics QuantaurusTau C11367 (Tables S4.1 and S4.2). Low temperature measurements were performed using a Unisoku CoolSpeK UV USP-203-B cryostat. All measurements were conducted using a 10-mm square quartz cell, unless otherwise noted. Bulk viscosity of the mixed system of hexadecane/mineral oil was measured at 25°C by using a DV2T touch screen viscometer (AMETEK Brookfield). Fluorescence microscope images were taken with a digital camera (Leica DFC450 C) connected to an upright microscope (Leica DM2700 P). To evaluate the photostability of compounds, a UV-LED light source (HAMATSU LIGHTSOURCETM LC-L1V3 equipped with C11924-111 and L11921-400, λ = 365 nm, 100 mW cm^{-2}) was used.

X-ray crystallography

X-ray crystallographic data of **FLAP1** and **FLAP2** were collected at −180 °C with a Rigaku XtaLAB P200 diffractometer equipped with a copper MicroMax007HF generator, VariMax-Cu optics, and a PILATUS 200K two-dimensional detector. The structure was solved by direct method SHELXT[S4] and refined by SHELXL[S5] programs. All non-hydrogen atoms were refined anisotropically and all hydrogen atoms were placed using AFIX instructions. Crystallographic data have been deposited in the Cambridge Crystallographic Data Center with the CCDC numbers of 2081297 (**FLAP1**) and 2081298 (**FLAP2**).

## 2. Synthesis of compounds

Synthesis of 2
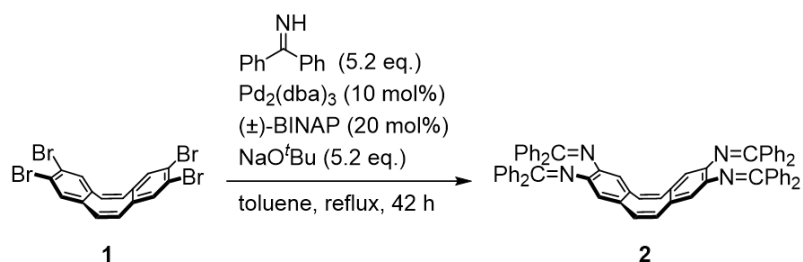
Pd$_2$(dba)$_3$ (630 mg, 690 μmol) and (±)-BINAP (920 mg, 1.4 mmol) were placed in a two-necked flask, and the flask was purged with argon. The mixture was dissolved with distilled toluene (170 mL), stirred at 110 °C for 30 min, and the solution was cooled to room temperature. Compound **1** (3.5 g, 6.7 mmol), NaO^{t}Bu (3.4 g, 35 mmol), and benzophenone imine (5.9 mL, 35 mmol) were added to the solution, and the mixture was refluxed for 42 h. The resulting mixture was cooled to room temperature, diluted with an excess amount of CHCl$_3$, and filtered through a Celite pad. The filtrate was evaporated to obtain a black residue. The residue was purified by silica gel column chromatography (CH$_2$Cl$_2$/hexane/Et$_3$N, 90:10:1) to obtain crude product as orange solid. Through continuous precipitation from CH$_2$Cl$_2$/MeOH and filtration, pure compound **2** was obtained as a yellow solid (5.0 g, 81%). ^{1}H NMR (CDCl$_3$, 600 MHz): δ (ppm) 7.66 (d, J = 7.2 Hz, 8H), 7.39 (t, J = 7.8 Hz, 4H), 7.32 (t, J = 7.8 Hz, 8H), 7.29 (t, J = 7.2 Hz, 4H), 7.19 (t, J = 7.5 Hz, 8H), 6.84 (d, J = 7.8 Hz, 8H), 6.21 (s, 4H), 6.10 (s, 4H); ^{13}C NMR (CDCl$_3$, 151 MHz) δ (ppm) 167.43, 140.35, 140.18, 136.83, 132.53, 132.44, 130.37, 129.54, 129.47, 128.78, 128.03, 127.94, and 121.94; HR-APCI-TOF-MS (m/z) found 920.3841, calcd for C$_{68}$H$_{48}$N$_4$: 920.3873 [M]$^+$.

Synthesis of 3
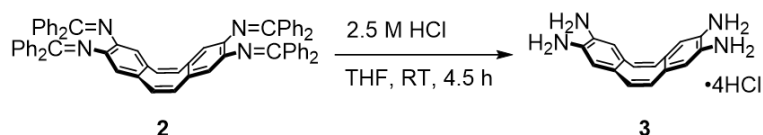
Compound **2** (5.0 g, 5.4 mmol) was placed in a two-necked flask, and the flask was purged with argon. To the flask, anhydrous THF (330 mL) and an aqueous solution of HCl (2.5 M, 11 mL) were added, and the reaction mixture was stirred at 25 °C for 4.5 h. The resulting suspension was collected by filtration under nitrogen flow and dried under vacuum, providing **3** as a white solid (2.5 g, quant.). The product was used for the next step without further purification and kept under argon atmosphere at –30 °C because of the poor stability in air. ^{1}H NMR (DMSO-d_6, 600 MHz): δ (ppm) 8.4–6.9 (very broad), 6.67 (s, 4H), 6.55 (s, 4H). ^{13}C NMR (DMSO-d_6, 151 MHz) δ (ppm) 132.14, 130.00, 128.58, and 120.8–120.0 (br).

Synthesis of FLAP1
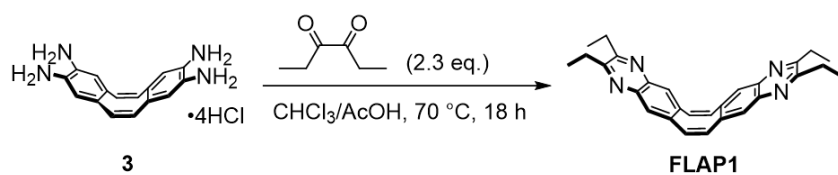
Compound **3** (150 mg, 370 mmol) was placed in a Schlenk flask, and the flask was purged with argon. To the flask, CHCl$_3$ (4.5 mL, N$_2$ bubbled), acetic acid (2.7 mL, N$_2$ bubbled), and 3,4-hexanedione (0.10 mL, 830 mmol) were added, and the resulting suspension was stirred at 70 °C for 18 h. The resulting mixture was cooled to room temperature and extracted with CHCl$_3$. The organic layer was washed with an aqueous NaHCO$_3$ solution, dried over anhydrous Na$_2$SO$_4$, and then evaporated. The crude product was purified by recrystallization from THF/MeOH to obtain pure **FLAP1** as a white solid (106 mg, 68%). ^{1}H NMR (CDCl$_3$, 600 MHz): δ (ppm) 7.74 (s, 4H), 7.10 (s, 4H), 2.96 (q, J = 7.2 Hz, 8H), 1.33 (t, J = 7.2 Hz, 12H); ^{13}C NMR (CDCl$_3$, 151 MHz): δ (ppm) 157.73, 139.93, 137.82, 133.21, 128.17, 28.75, and 12.57; HR-APCI-TOF-MS (m/z) found 420.2306, calcd for C$_{28}$H$_{28}$N$_4$: 420.2308 [M]$^+$.

Synthesis of FLAP2
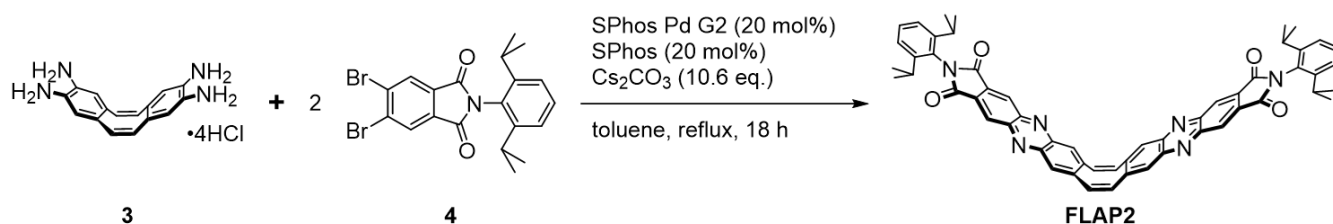
Compound **4** (130 mg, 290 μmol), SPhos Pd G2 (21 mg, 29 μmol), SPhos (12 mg, 29 μmol), Cs$_2$CO$_3$ (510 mg, 1.6 mmol), and compound **3** (60 mg, 150 μmol) were placed in a Schlenk flask, and the flask was purged with argon. To the flask, distilled toluene (2.3 mL) was added, then the resulting suspension was refluxed for 18 h. The resulting mixture was cooled to room temperature and filtrated through a Celite® pad. The resulting solution was evaporated under reduced pressure, and the residue was purified by a flash silica-gel column chromatography (eluent: CHCl$_3$/EtOAc (1:1)) for two times. The crude product was reprecipitated from CHCl$_3$/MeOH for three times to obtain pure **FLAP2** as a yellow solid (35.4 mg, 28%). ^{1}H NMR (CDCl$_3$, 600 MHz): δ (ppm) 8.78 (s, 4H), 8.19 (s, 4H), 7.49 (t, J = 7.8 Hz, 2H), 7.38 (s, 4H), 7.32 (d, J = 7.8 Hz, 4H), 2.73 (sep, J = 6.8 Hz, 4H), 1.18 (d, J = 6.8 Hz, 24H); ^{13}C NMR (CDCl$_3$, 151 MHz): δ (ppm) 166.66, 146.96, 145.52, 143.37, 141.44, 133.49, 131.01, 130.64, 129.65, 127.83, 126.97, 124.27, 29.60, and 24.15; HR-APCI-TOF-MS (m/z) found 866.3607, calcd for C$_{56}$H$_{46}$N$_6$O$_4$: 866.3586 [M]$^-$.

Attempted synthesis of 5
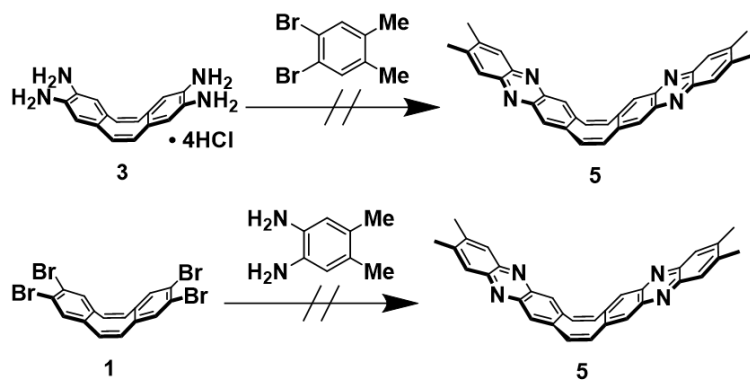
Figure S2.1. Schemes for the synthesis of **5**. We attempted to synthesize **5** by applying the same reaction conditions in the synthesis of **FLAP2**. The coupling partners of **3** and 1,2-dibromo-4,5-dimethylbenzene, as well as **1** and 4,5-dimethylbenzene-1,2-diamine, were used for the reaction, but **5** was not obtained in this reaction condition probably because the reaction stopped halfway due to the poor solubility.

3. Characterization of new compounds

3.1. ¹H and ¹³C NMR spectroscopy
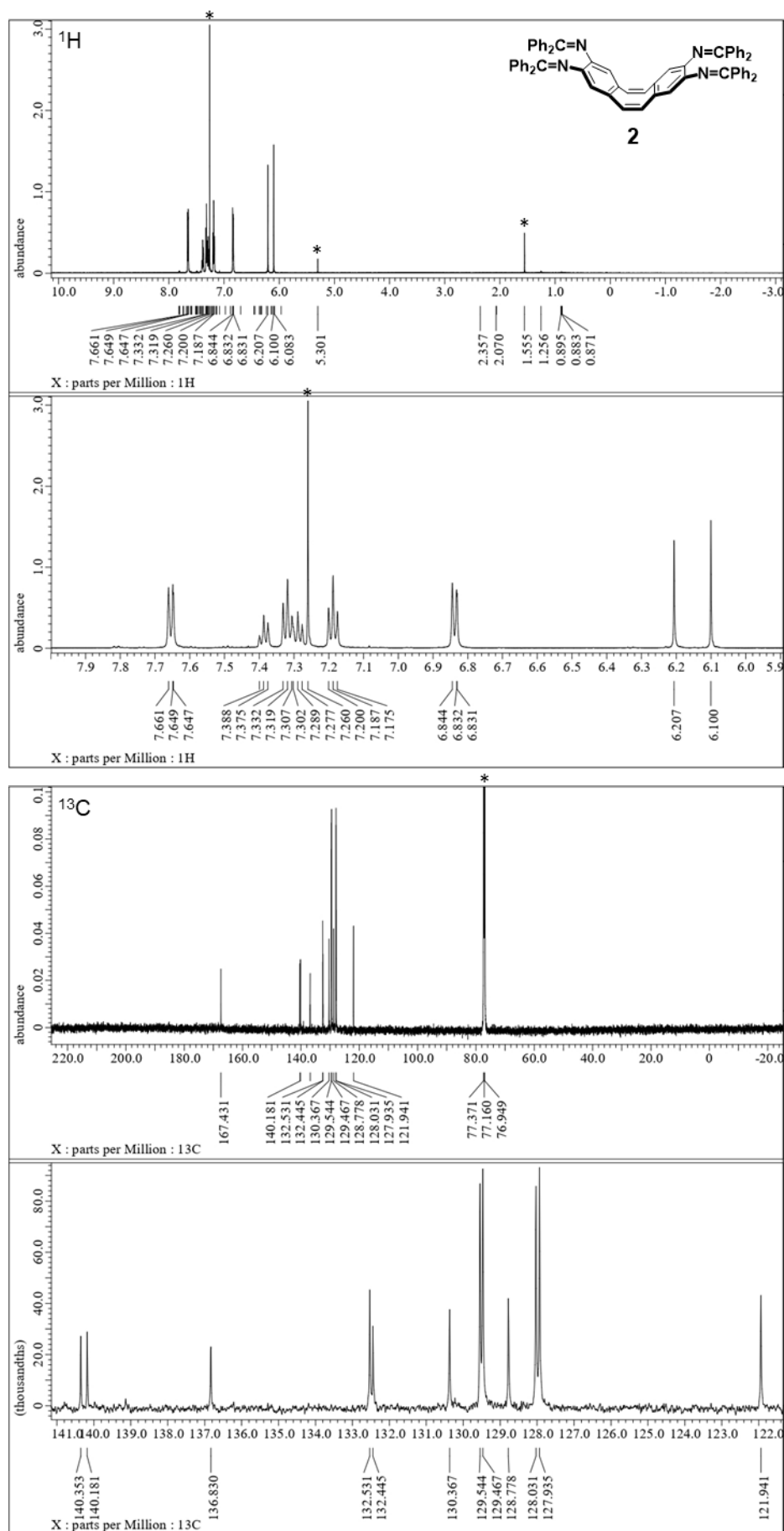
Figure S3.1. ¹H NMR (top) and ¹³C NMR (bottom) spectra of **2** in CDCl₃. Signals marked with asterisk (*) indicate residual solvents.
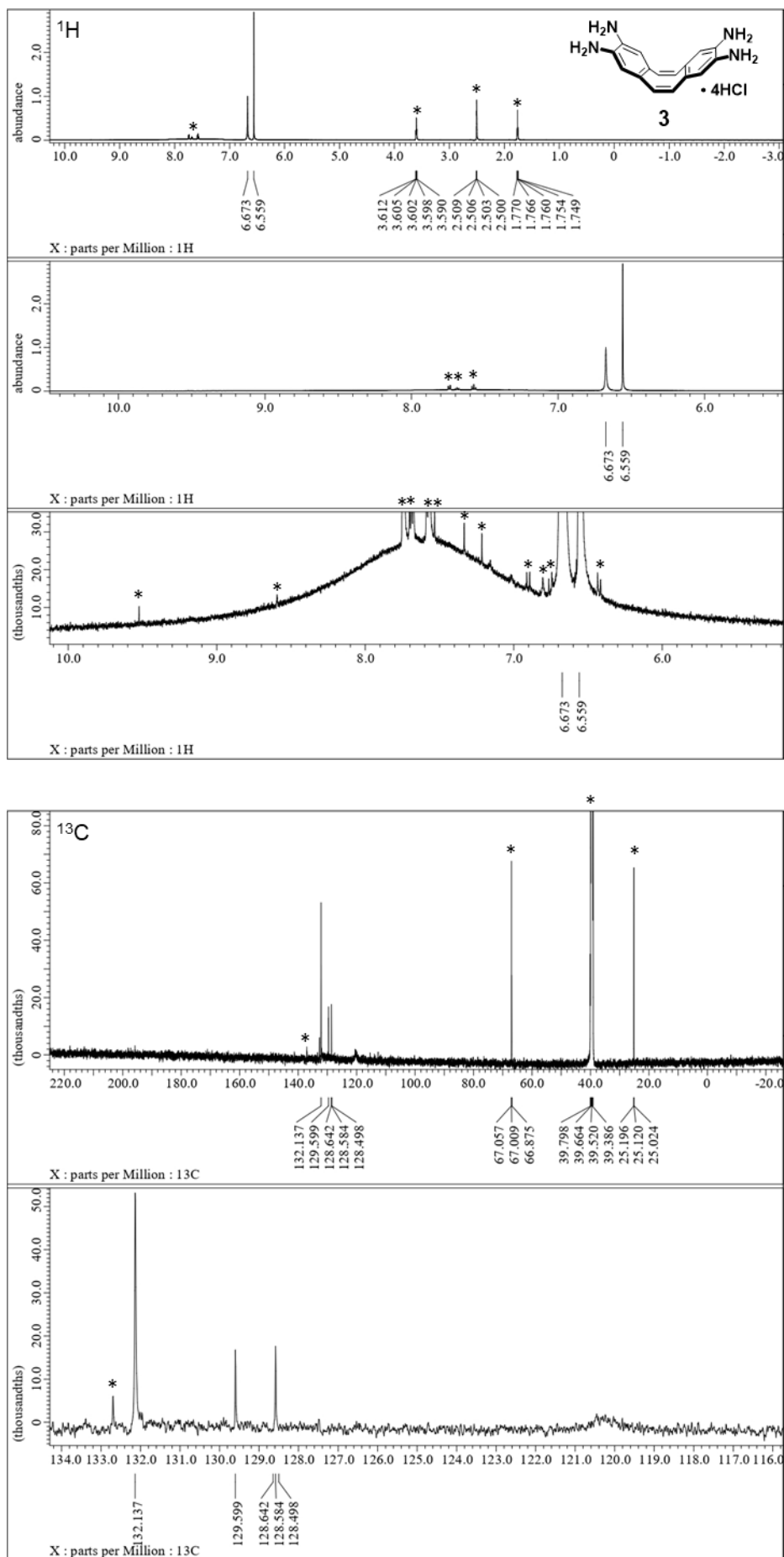
Figure S3.2. ^{1}H NMR (top) and ^{13}C NMR (bottom) spectra of **3** in DMSO-d_6. Signals marked with asterisk (*) indicate residual solvents and impurities.
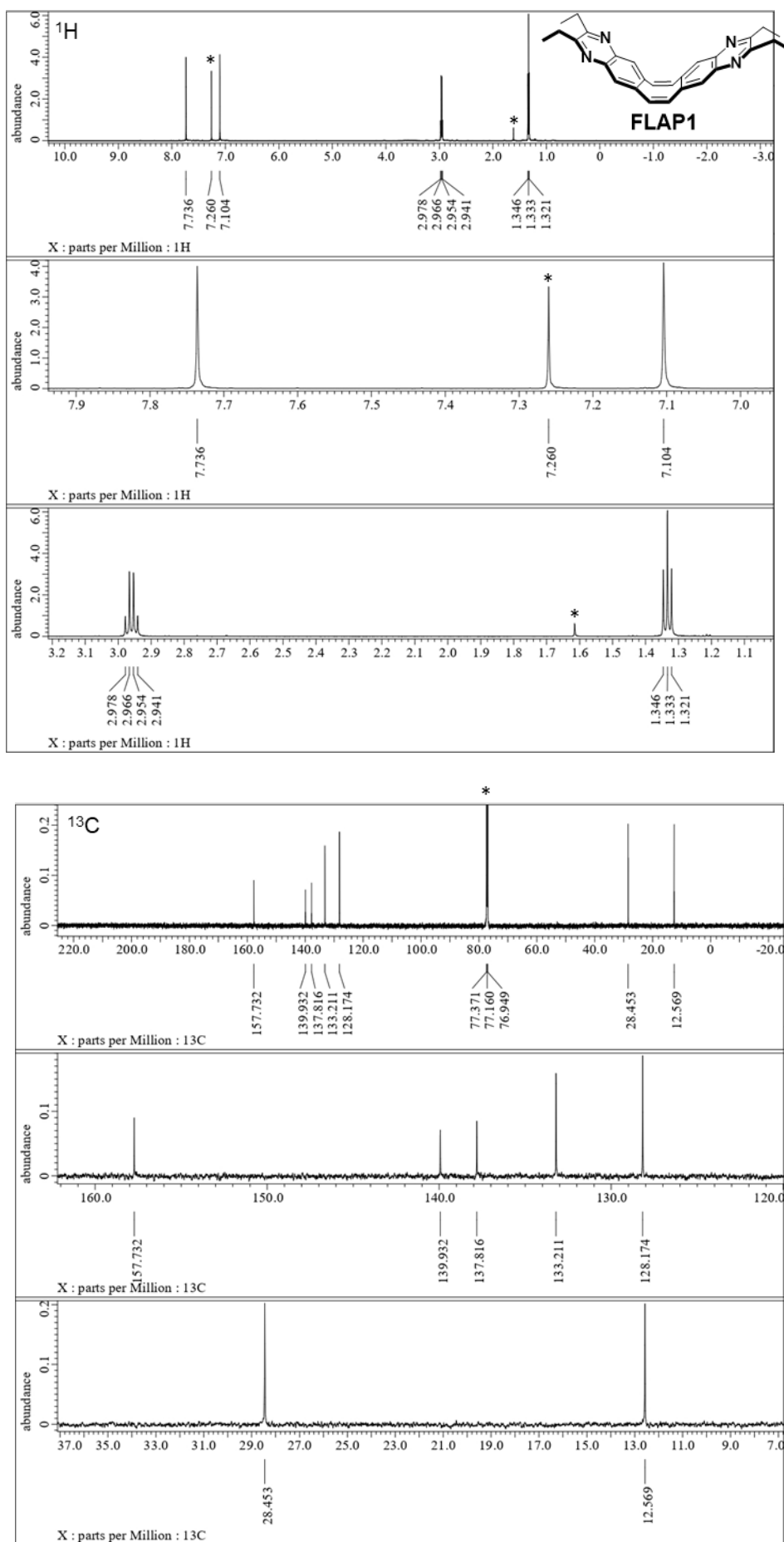
Figure S3.3. ¹H NMR (top) and ¹³C NMR (bottom) spectra of **FLAP1** in CDCl₃. Signals marked with asterisk (*) indicate residual solvents.
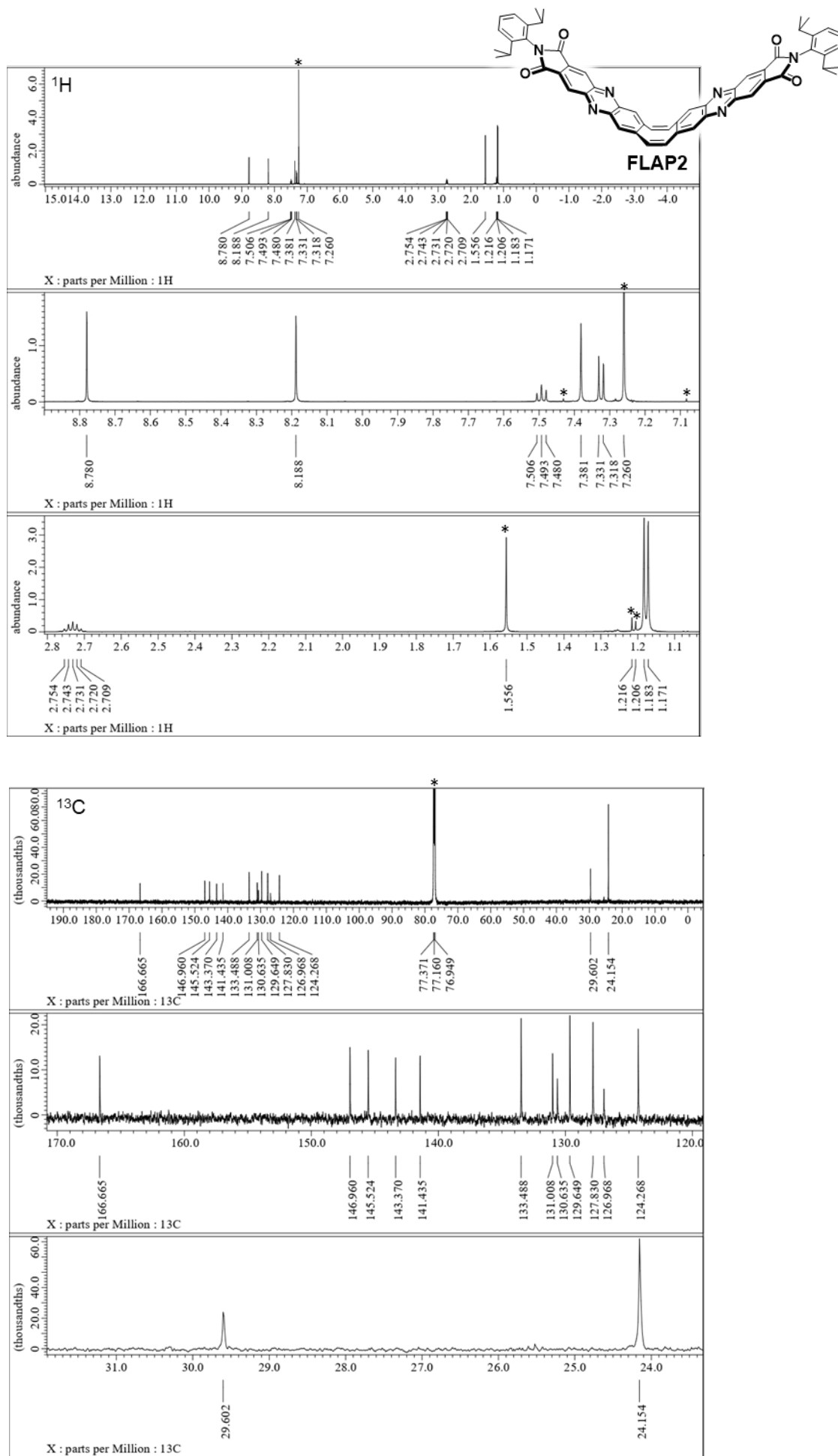
Figure S3.4. ^{1}H NMR (top) and ^{13}C NMR (bottom) spectra of **FLAP2** in CDCl$_3$. Signals marked with asterisk (*) indicate residual solvents and impurities.

3.2. High resolution mass spectrometry
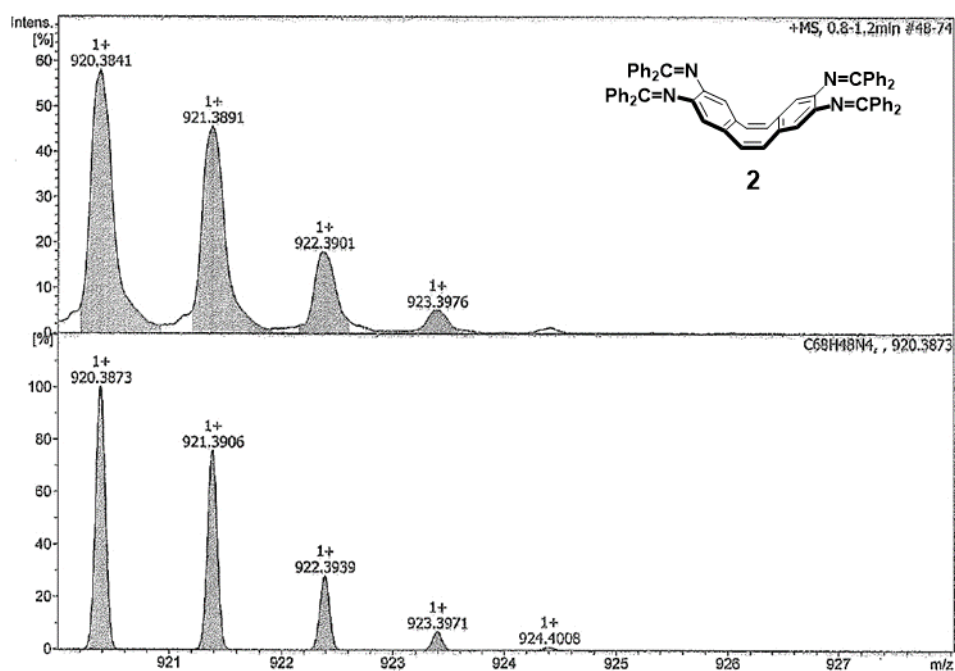
Figure S3.5. HR-APCI-TOF-MS (positive mode) of **2** (top: observed, bottom: simulated).
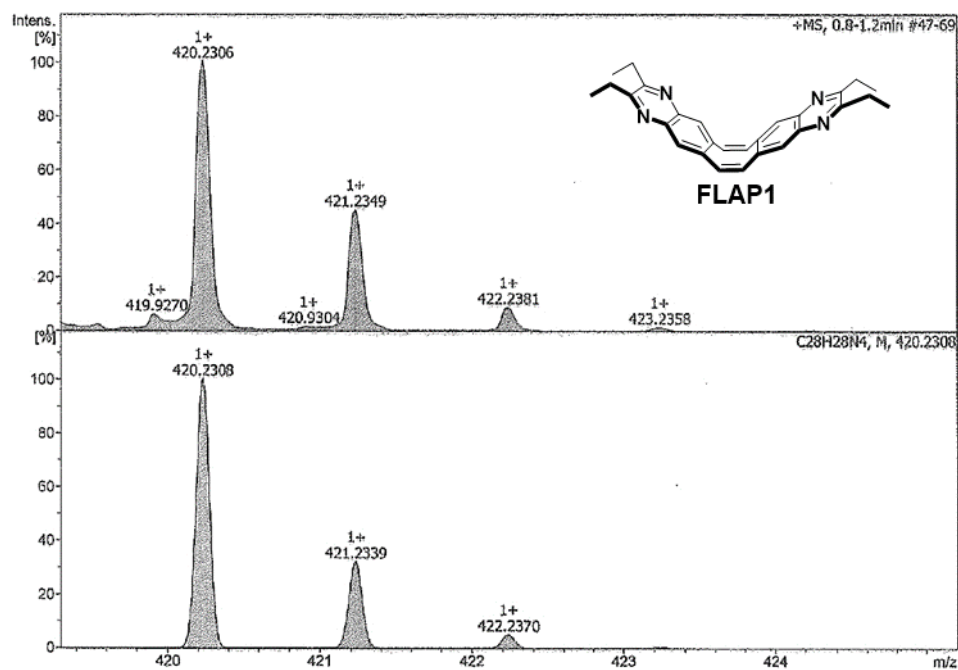
Figure S3.6. HR-APCI-TOF-MS (positive mode) of **FLAP1** (top: observed, bottom: simulated).
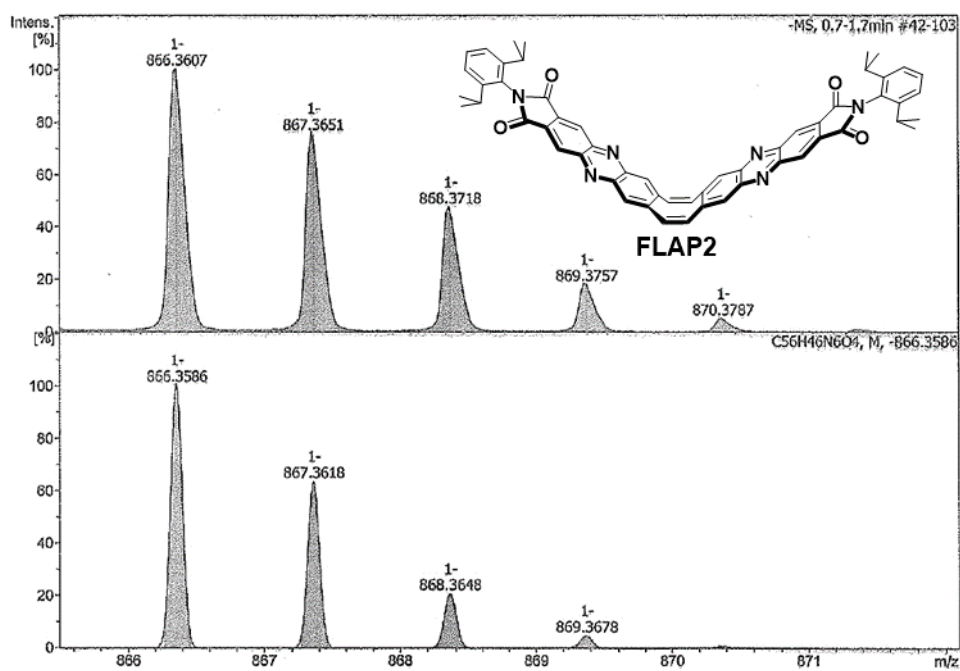
Figure S3.7. HR-APCI-TOF-MS (negative mode) of **FLAP2** (top: observed, bottom: simulated).

4. Photophysical properties

4.1. UV-visible absorption and fluorescence spectra
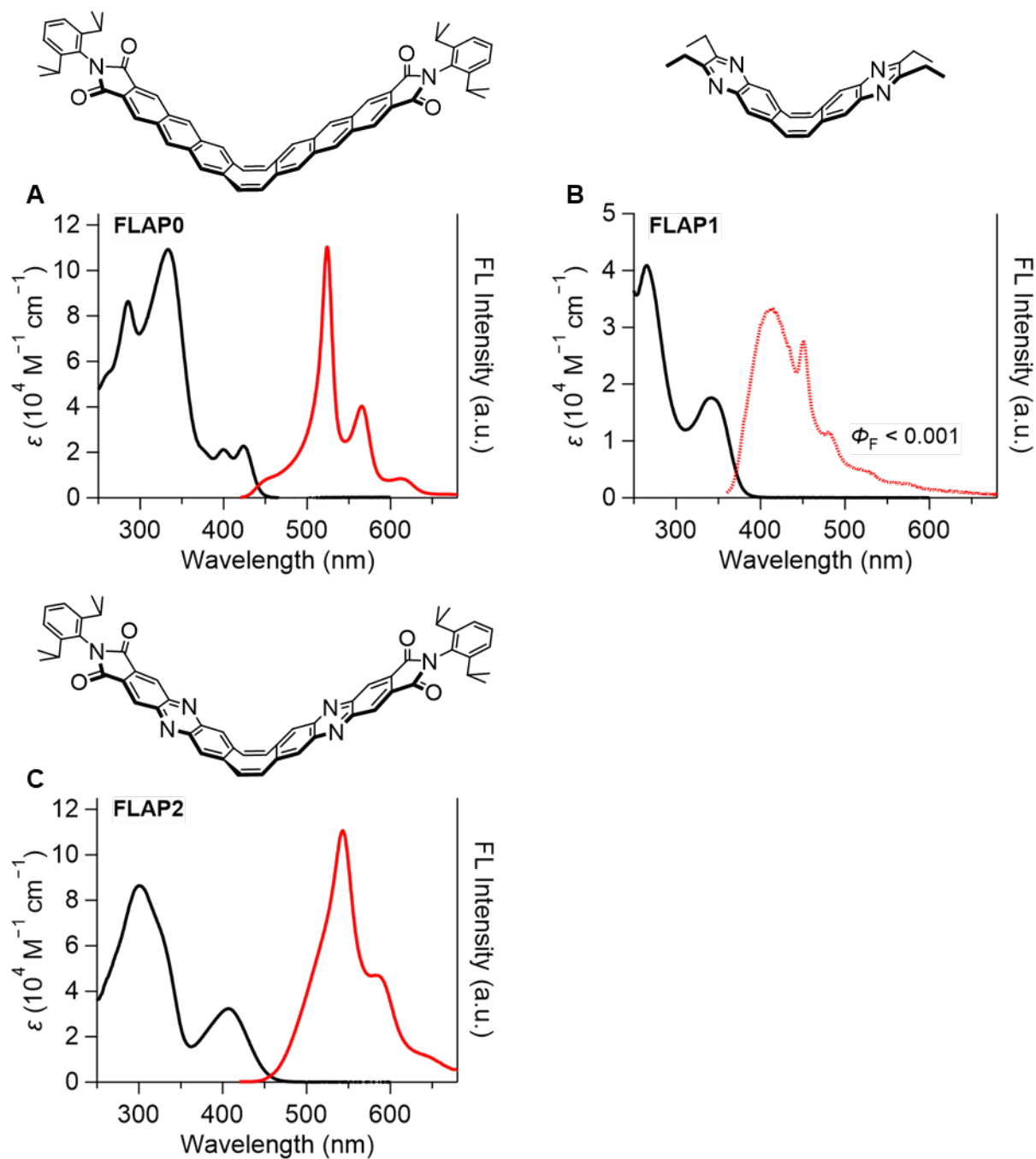
Figure S4.1. UV-visible absorption (black line) and fluorescence (red line) spectra of (**A**) **FLAP0**, (**B**) **FLAP1**, (**C**) **FLAP2** in CHCl₃ (excitation wavelength λ_{ex} = 340 nm for **FLAP1**, λ_{ex} = 400 nm for **FLAP0** and **FLAP2**).

4.2. Solvent dependence
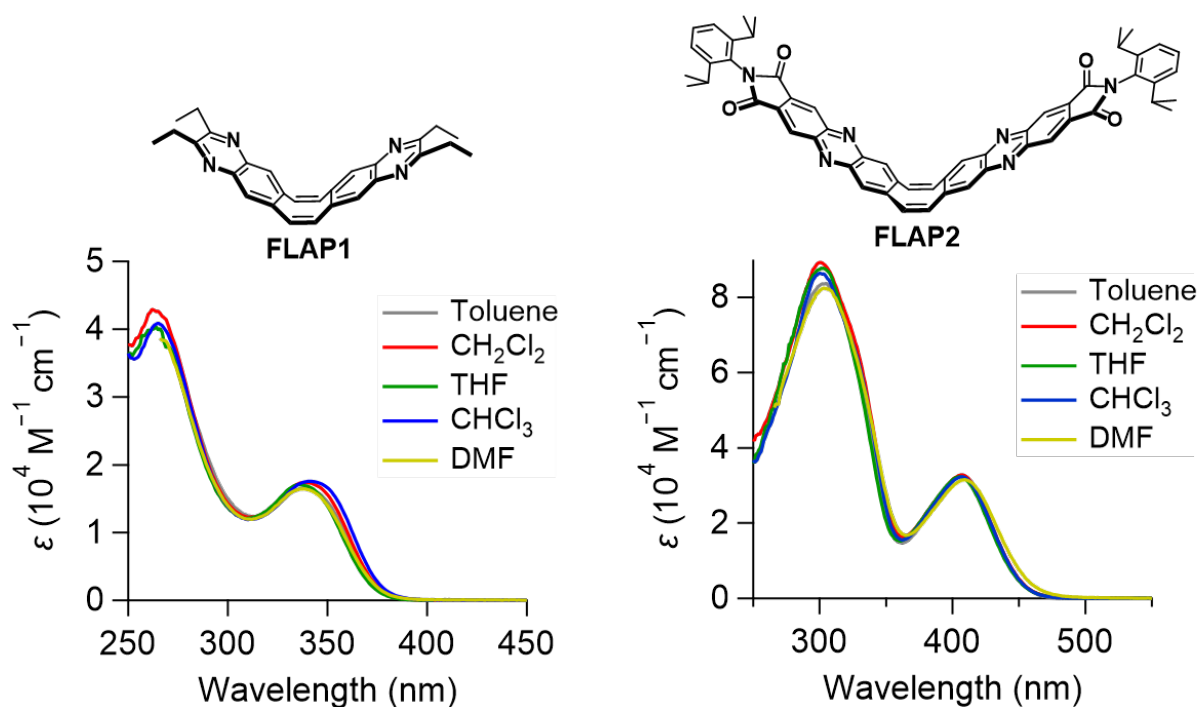
Figure S4.2. UV-visible absorption spectra of **FLAP1** and **FLAP2** in various solvents with the concentration of 8×10^{-6} M.
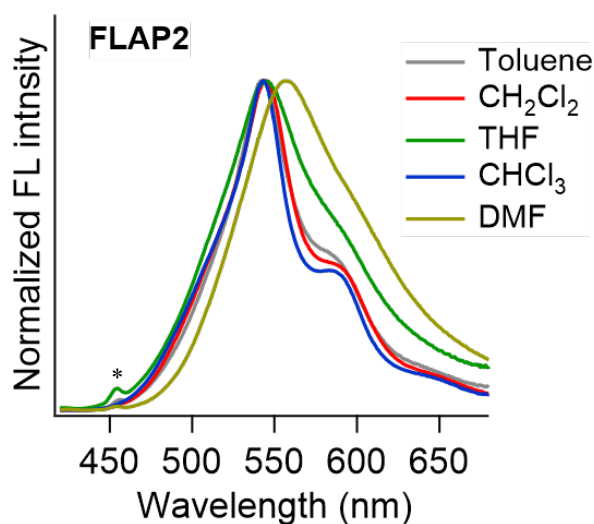
Figure S4.3. Fluorescence spectra of **FLAP2** in various solvents with the concentration of 8×10^{-6} M (excitation wavelength $\lambda_{ex} = 340$ nm). Peaks marked with asterisk (*) indicate Raman peaks delivered from the solvent.
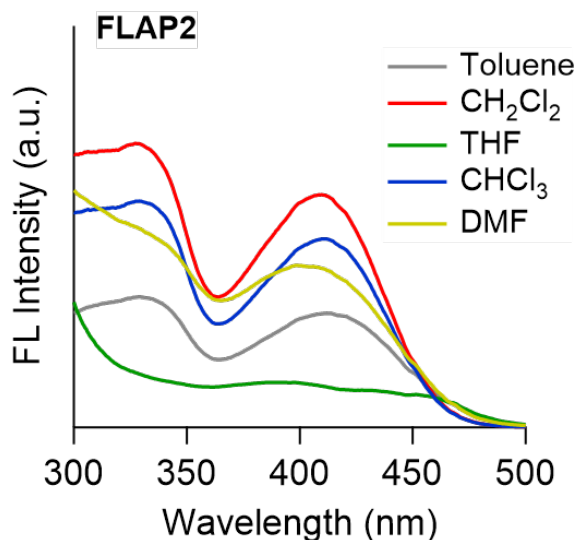
Figure S4.4. Excitation spectra of **FLAP2** in various solvents with the concentration of 8×10^{-6} M (emission wavelengths $\lambda_{em} = 545$ nm).

Table S4.1. Absolute FL quantum yield Φ_F of **FLAP1** in various solvents (excitation wavelength $\lambda_{ex} = 340$ nm).

	Φ_F
Toluene	<0.001
CH$_2$Cl$_2$	<0.001
THF	<0.001
CHCl$_3$	<0.001
DMF	<0.001

Table S4.2. Absolute FL quantum yield Φ_F and FL lifetime τ_F of **FLAP2** in various solvents or a PMMA matrix

	Φ_F	τ_F	χ^2
Toluene	0.015	490 ps	4.10 (1st order fitting)
		480 ps (>99%), 2.5 ns (0.4%)	1.10 (2nd order fitting)
CH$_2$Cl$_2$	0.028	480 ps	1.31 (1st order fitting)
THF	0.017	480 ps	6.48 (1st order fitting)
		430 ps (>99%), 1.9 ns (0.8%)	1.18 (2nd order fitting)
CHCl$_3$	0.021	500 ps	1.31 (1st order fitting)
DMF	0.061	890 ps	1.04 (1st order fitting)
PMMA	0.012	1.1 ns	76.4 (1st order fitting)
		530 ps (92%), 3.0 ns (8%)	6.32 (2nd order fitting)
		290 ns (80%), 1.3 ns (19%), 5.3 ns (2%)	1.32 (3rd order fitting)

Excitation wavelength $\lambda_{ex} = 400$ nm for Φ_F, and 405 nm for τ_F. Emission wavelength $\lambda_{em} = 515$ nm (PMMA) and 545 nm (other solvents) for τ_F. The PMMA matrix was prepared by the following method: **FLAP1** (0.1 wt%) and PMMA (typical M_w = 15000, Aldrich) were dissolved in toluene, and this solution was dropped onto a quartz plate and dried under vacuum for 12 h.
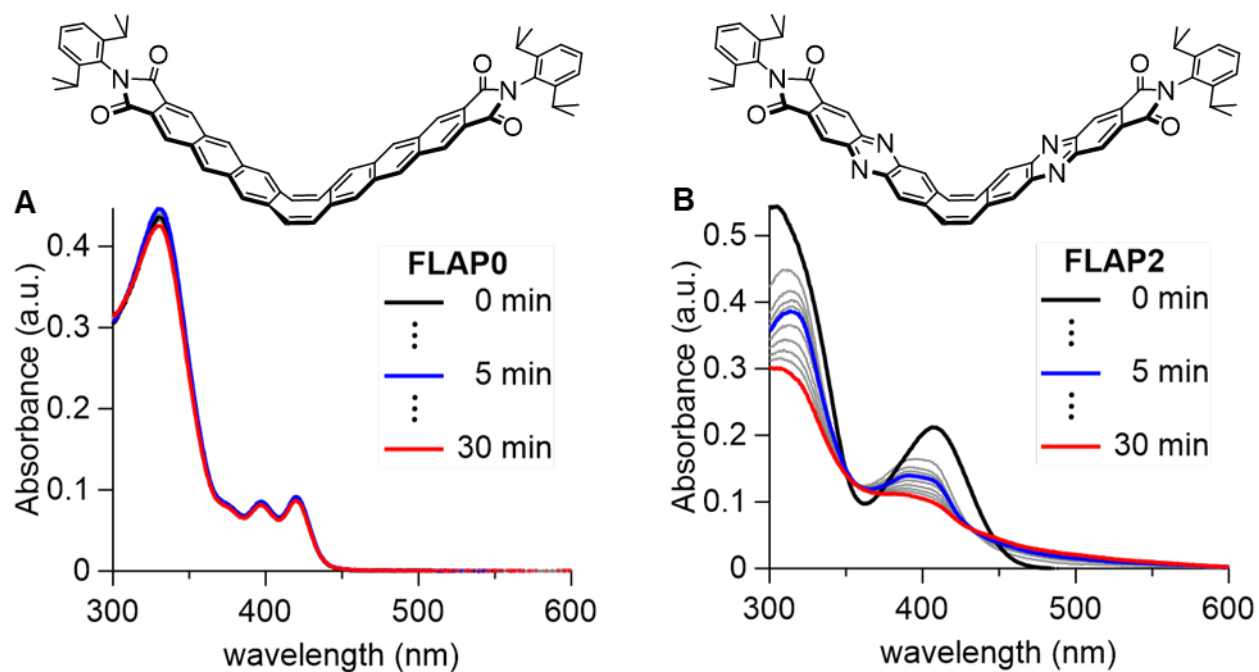
4.3. Photostability under UV irradiation

Figure S4.5. Evaluation of photostability of (**A**) **FLAP0** and (**B**) **FLAP2**. Concentration of **FLAP0** and **FLAP2** in $CHCl_3$ was adjusted with the absorbance of 0.1 at 365 nm. The $CHCl_3$ solutions were stirred under continuous spot irradiation using a UV-LED light source ($\lambda = 365$ nm, 100 mW cm^{-2}). Photodegradation was monitored by absorption spectroscopy of the solutions.

4.4. Fluorescence spectra in the mixed solvent system of DMSO/glycerol
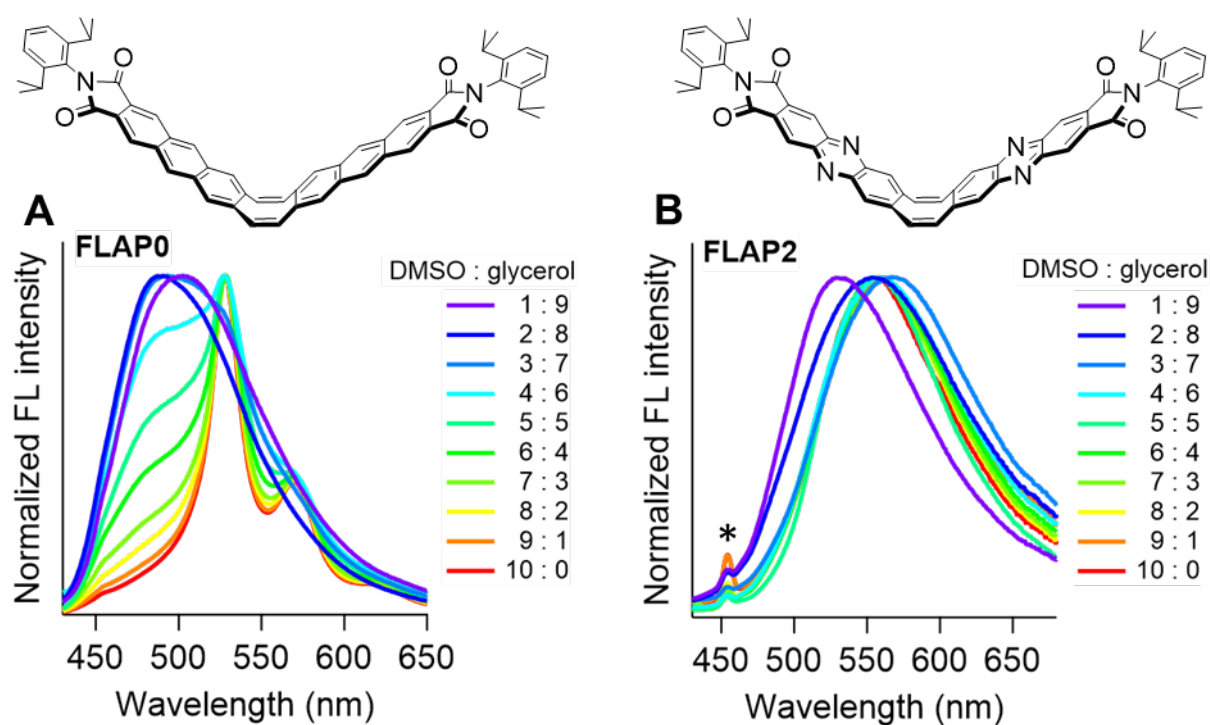
Figure S4.6. Viscosity-dependent fluorescence spectra of (**A**) **FLAP0** and (**B**) **FLAP2** in the mixed solvent system of DMSO/glycerol. The viscosity values of the mixed system were referenced from the literature[S7], in which 668 (1:9), 338 (2:8), 169 (3:7), 86.4 (4:6), 44.9 (5:5), 23.7 (6:4), 12.8 (7:3), 7.0 (8:2), 3.9 (9:1), and 2.2 cP (10:0), respectively. Excitation wavelength λ_{ex} = 340 nm. Peaks marked with asterisk (*) indicate Raman peaks delivered from the solvent.

4.5. Temperature dependence
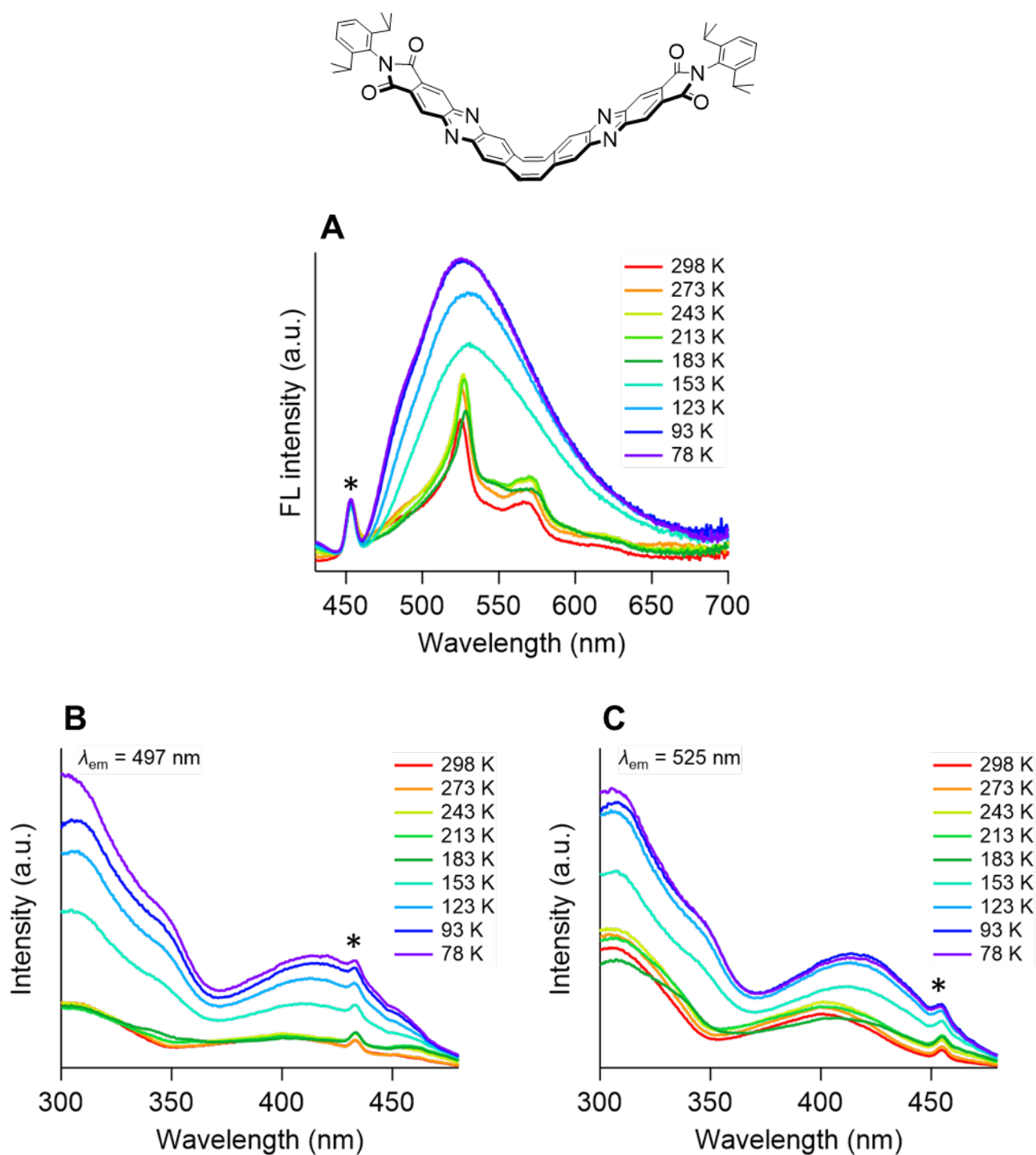
Figure S4.7. (A) Temperature dependent fluorescence spectra of **FLAP2** in 3-methylpentane (melting point: –118 °C). Excitation wavelength λ_{ex} = 400 nm for all measurements. **(B, C)** Temperature dependent excitation spectra of **FLAP2** in 3-methylpentane. Emission wavelengths: **(B)** 497 nm and **(C)** 525 nm. Peaks marked with asterisk (*) indicate Raman peaks delivered from the solvent.

4.6. Fluorescence of the crystals
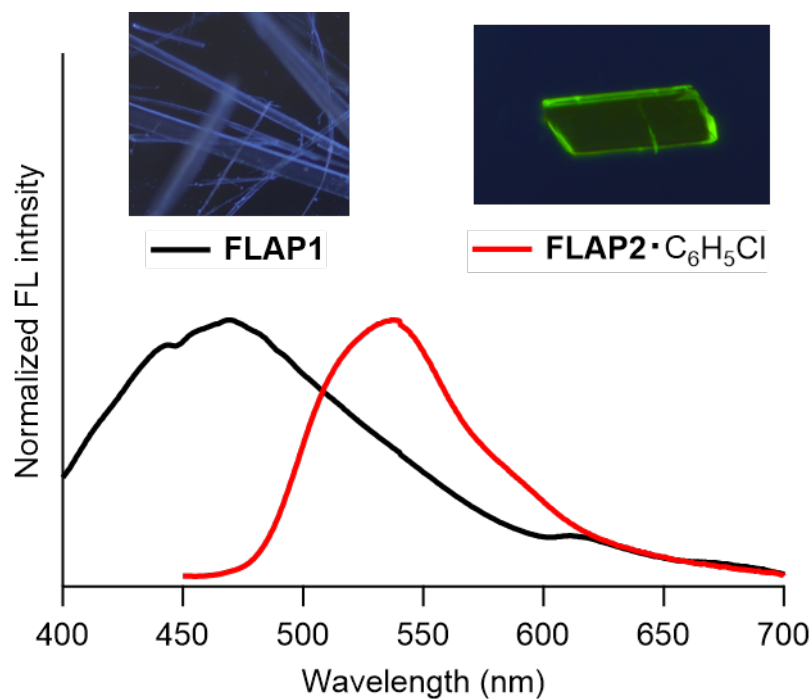
Figure S4.8. Fluorescence spectra of the crystals **FLAP1** and **FLAP2**•C_6H_5Cl.

4.7. Fluorescence in a PMMA matrix
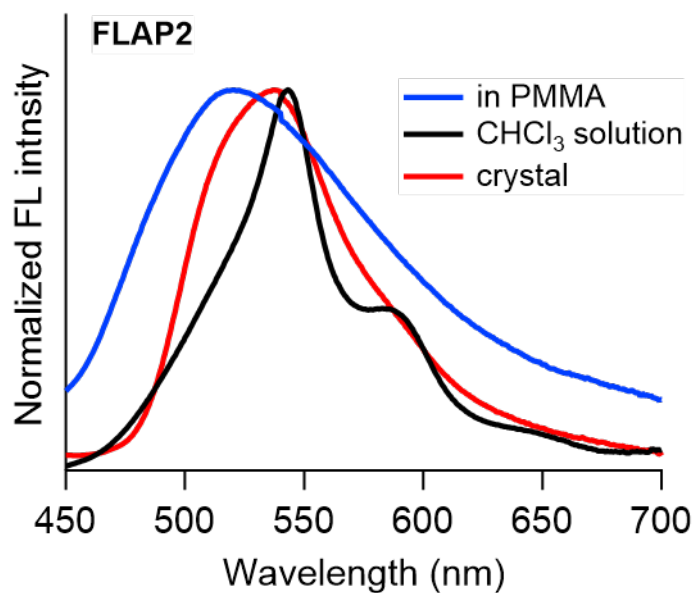
Figure S4.9. Fluorescence spectra of **FLAP2** in a PMMA matrix, in a $CHCl_3$ solution, and in the crystalline phase. The preparation method for the PMMA matrix is described in Table 6.2.

5. X-ray crystallographic analysis

Figure S5.1. (A) Crystal structure of **FLAP1** from different views. Thermal ellipsoids are scaled to 50% probability. Hydrogen atoms are omitted for clarity. **(B)** Representative bond lengths (Å) and bond angles (°) and **(C)** COT bending angles (see **Figure S6.2** for the definition).

Figure S5.2. (**A**) Crystal structure of **FLAP2** from different views. Thermal ellipsoids are scaled to 50% probability. Hydrogen atoms and solvent molecules are omitted for clarity. (**B**) Representative bond lengths (Å) and bond angles (°) and (**C**) COT bending angles (see **Figure S6.2** for the definition). The 2,6-diisopropylphenyl groups are omitted for clarity.

Table S5.1. Crystal Data of **FLAP1** and **FLAP2**

	FLAP1	FLAP2
Formula	$C_{28}H_{28}N_4$	$C_{56}H_{46}N_6O_4 \cdot 2(C_6H_5Cl)$
FW	420.54	1092.08
Crystal system	triclinic	triclinic
Space Group	P-1 (No.2)	P-1 (No.2)
a / Å	4.6738(1)	8.7565(1)
b / Å	15.5587(5)	16.9417(3)
c / Å	16.6456(5)	20.1692(4)
α / °	68.373(3)	68.493(2)
β / °	88.012(2)	82.020(1)
γ / °	81.681(2)	81.345(1)
V / Å^3	1113.16(6)	2740.66(9)
Z	2	2
T / K	93	93
R_1 [$I>2\sigma(I)$]	0.0494	0.0800
wR_2 (all data)	0.1432	0.2317
GOF	1.057	1.027
CCDC No.	2081297	2081298

6. Theoretical calculations

Model structures **FLAP0′**, **FLAP1′**, and **FLAP2′** were calculated, which have hydrogen atoms in place of the ethyl groups and 2,6-diisopropylphenyl groups of the corresponding compounds (Figure S6.1). All calculations were performed at the (TD) PBE0/6-31+G(d) level of theory, using the Gaussian 16 program[S8]. All energy minimum structures had no imaginary frequency. The COT bending angle was defined as the dihedral angle between the C1–C2–C3 and C2–C3–C4 planes in Figure S6.2. The x, y, and z axes were defined as Figure S6.3 when a molecule has C_{2v} symmetry.
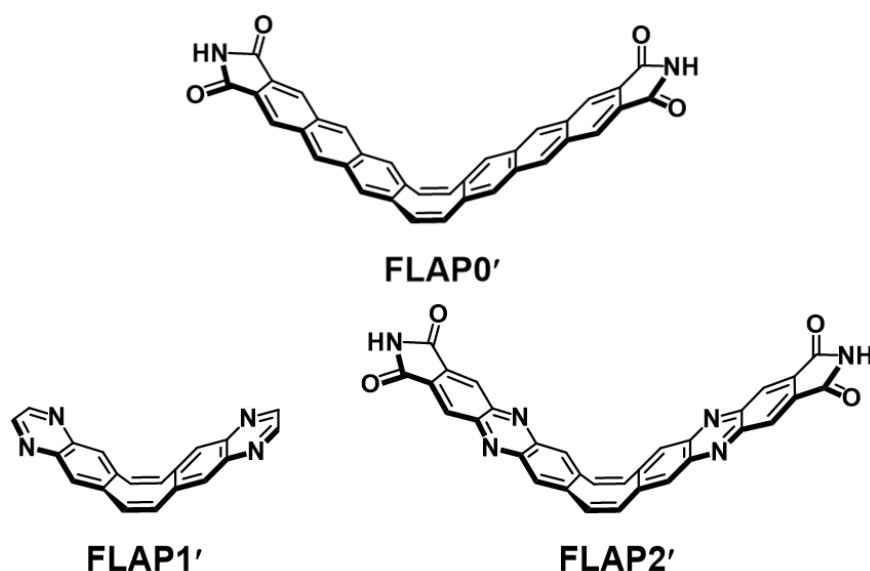
Figure S6.1. Structures of **FLAP0′**, **FLAP1′**, and **FLAP2′**.
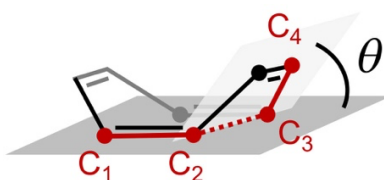
Figure S6.2. Definition of the COT bending angle.
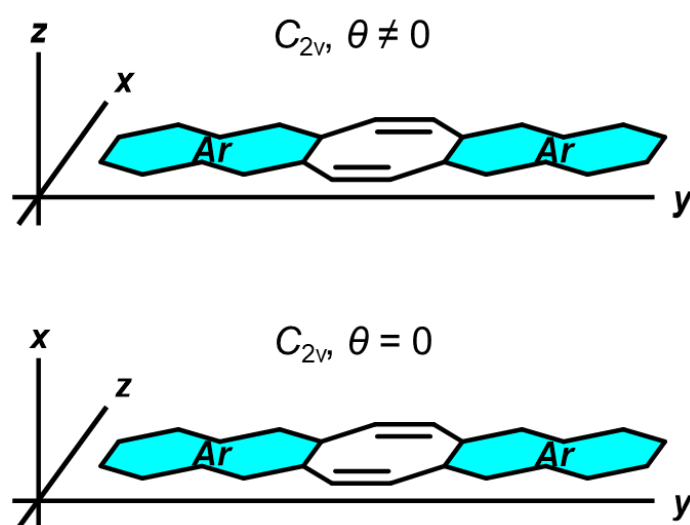
Figure S6.3. Definition of each axes.

6.1. Energetically close excited states at the different planar geometries optimized in S_1
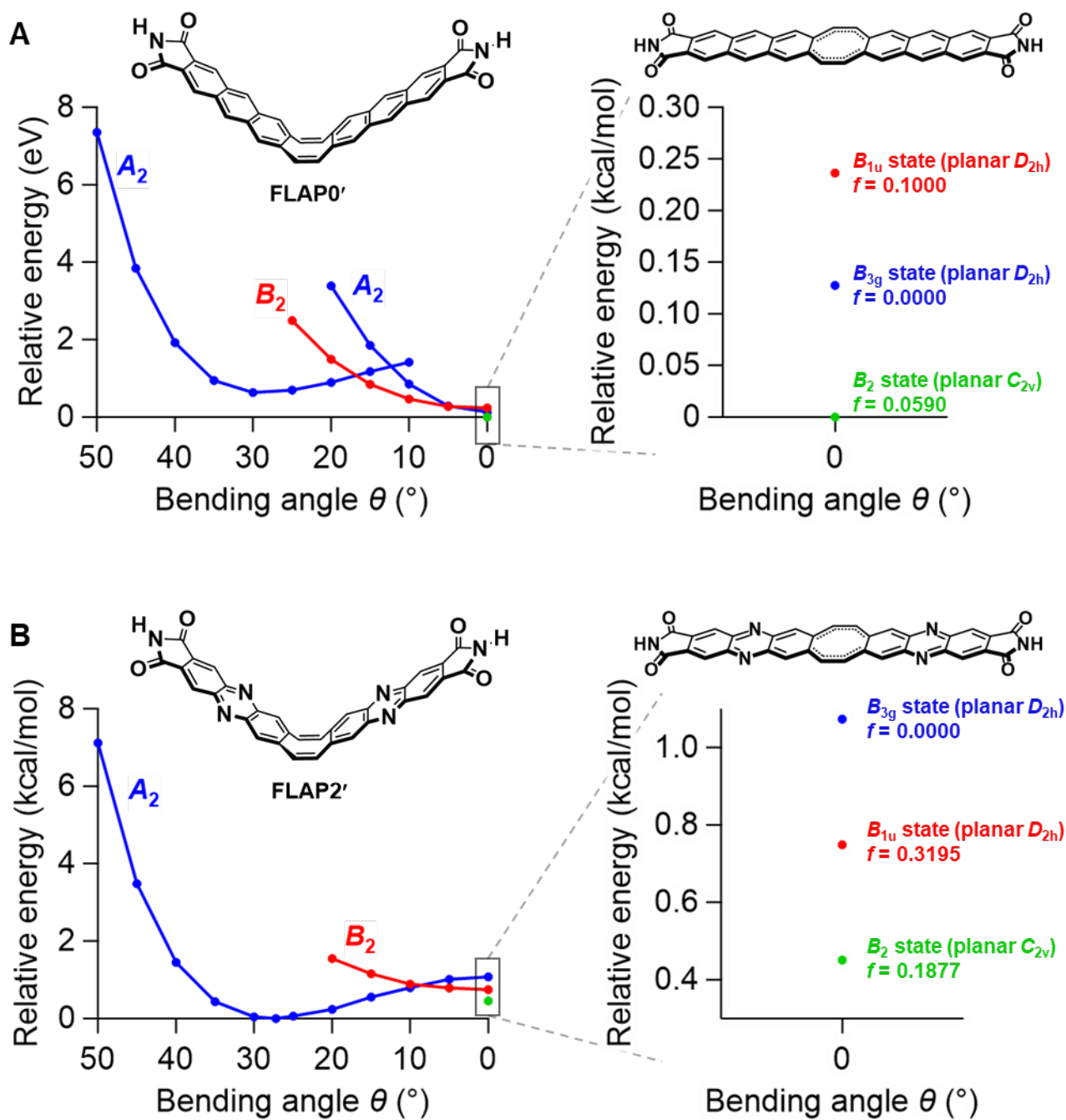
Figure S6.4. Energetically close excited states at $\theta = 0$, calculated with different S_1 optimized geometries (See the following pages).

(**A**) Three states of **FLAP0′** were obtained, as shown in Figure S6.6 (B_2), S6.7 (B_{1u}), and S6.8 (B_{3g}), respectively.

(**B**) Three states of **FLAP2′** were obtained, as shown in Figure S6.12 (B_2), S6.13 (B_{1u}), and S6.14 (B_{3g}), respectively.

6.2. Optimized geometries in S_0 and S_1
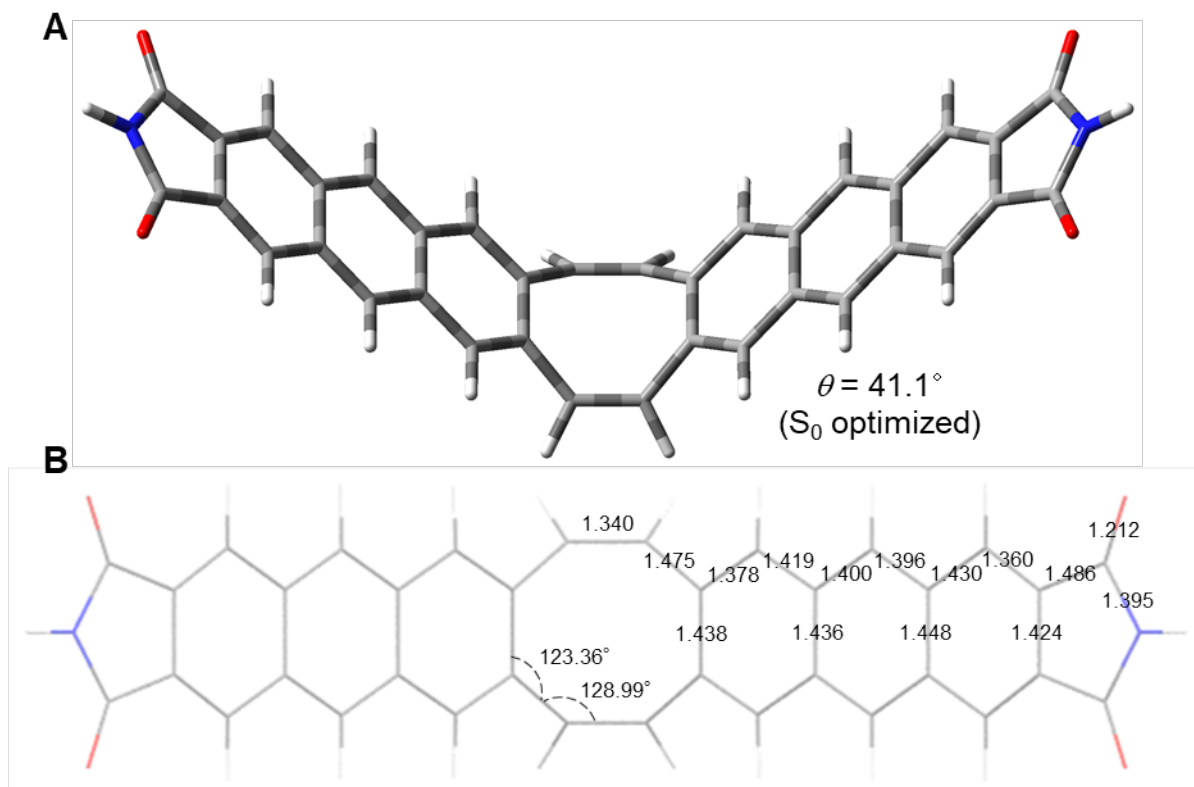
Figure S6.5. (**A**) S_0 optimized geometry of **FLAP0′** with bent C_{2v} symmetry (See Figure S6.15). (**B**) Representative bond lengths (Å) and bond angles.
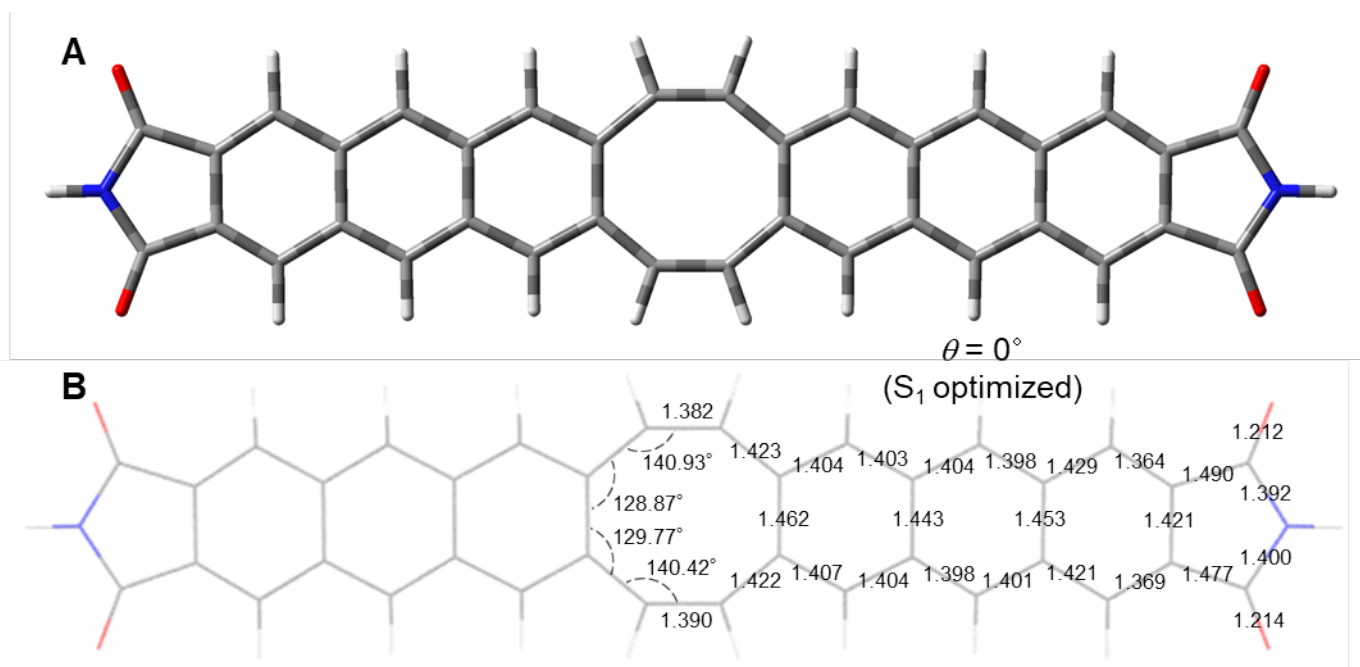
Figure S6.6. (**A**) S_1 optimized geometry of **FLAP0′** with planar C_{2v} symmetry that provides a B_2 state for the S_1 configuration (See Figure S6.4 and S6.16A). (**B**) Representative bond lengths (Å) and bond angles.
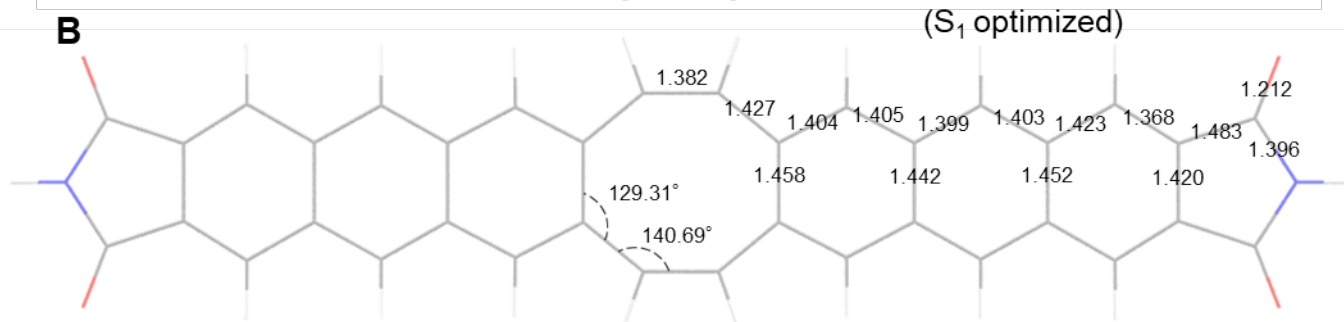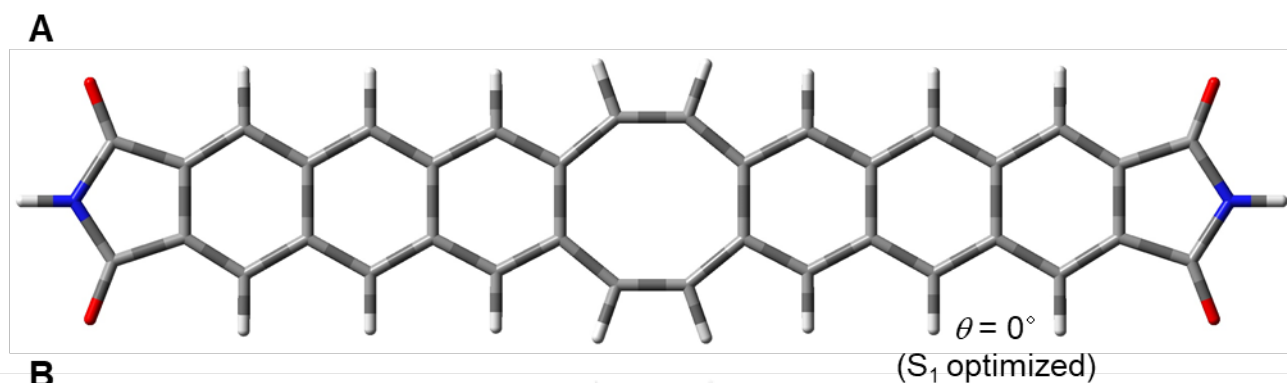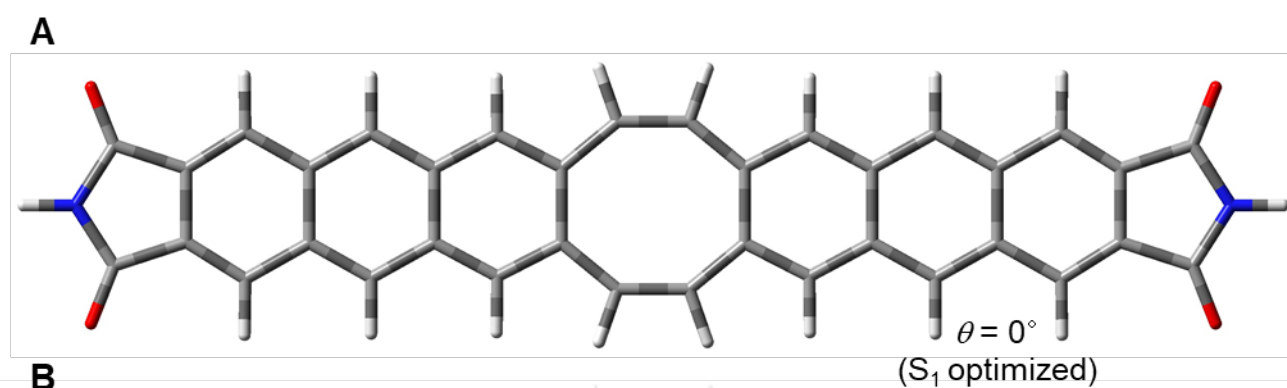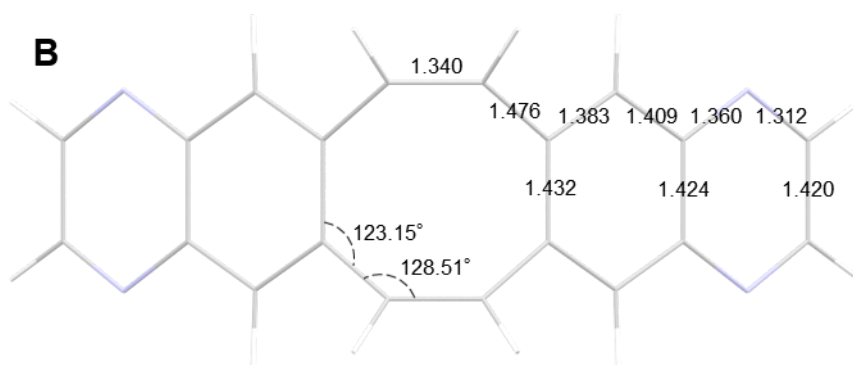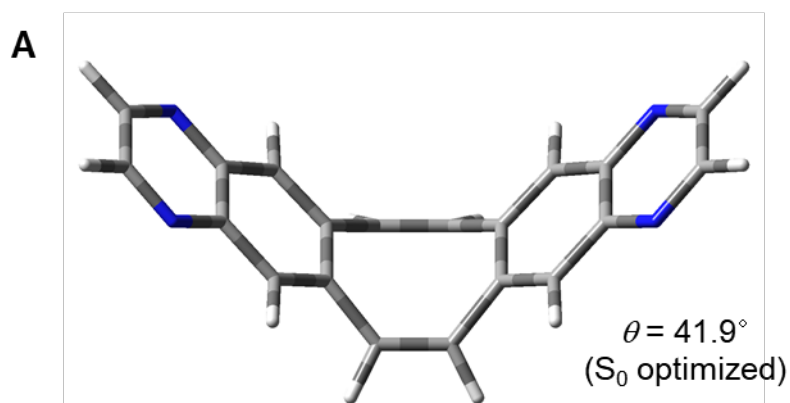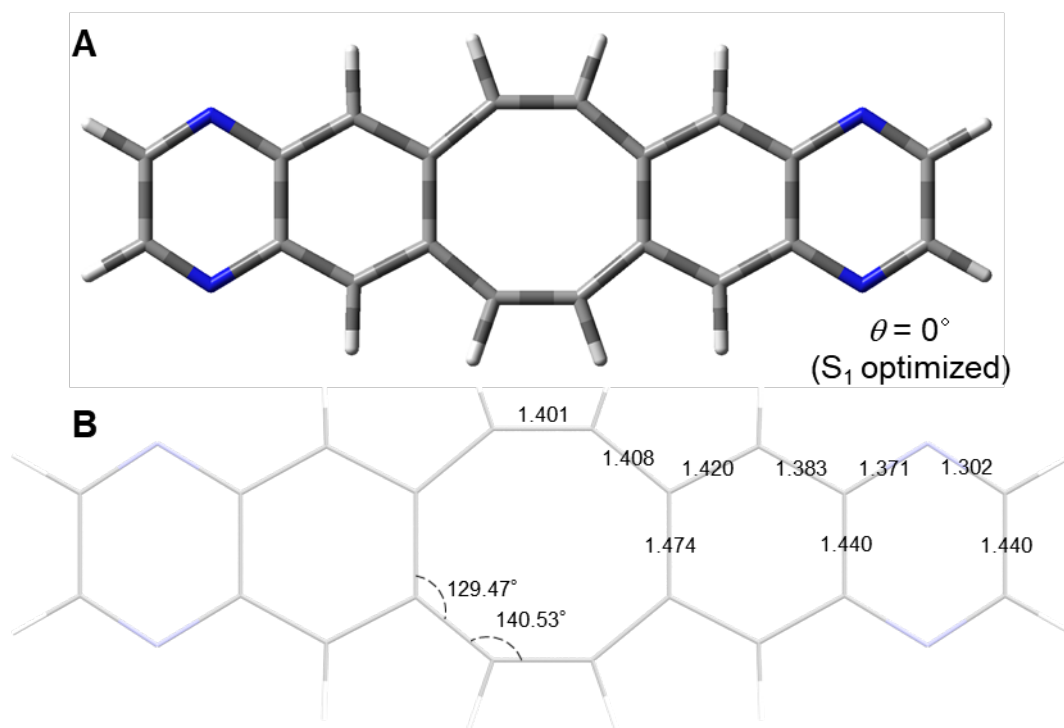
Figure S6.7. (A) S$_1$ optimized geometry of **FLAP0′** with planar D_{2h} symmetry that provides a B_{1u} state for the S$_1$ configuration (See Figure S6.4 and S6.16B). (B) Representative bond lengths (Å) and bond angles.
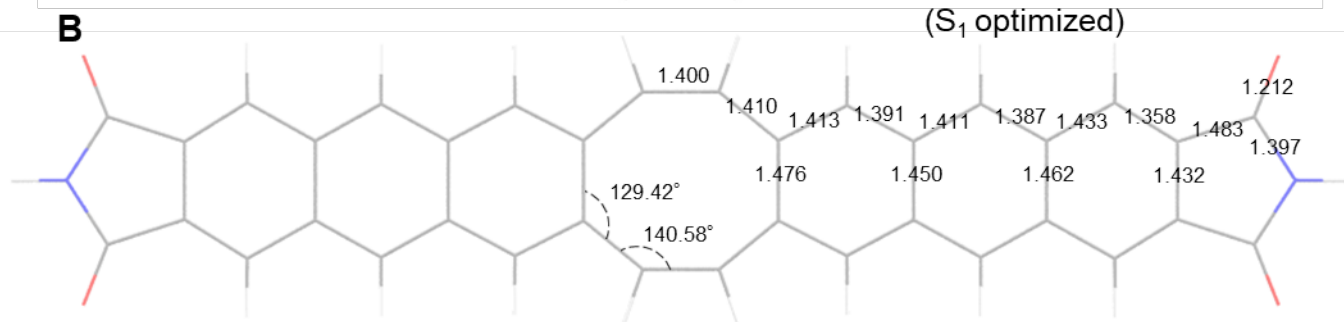
Figure S6.8. (A) S$_1$ optimized geometry of **FLAP0′** with planar D_{2h} symmetry that provides a B_{3g} state for the S$_1$ configuration (See Figure S6.4 and S6.16C). (B) Representative bond lengths (Å) and bond angles.
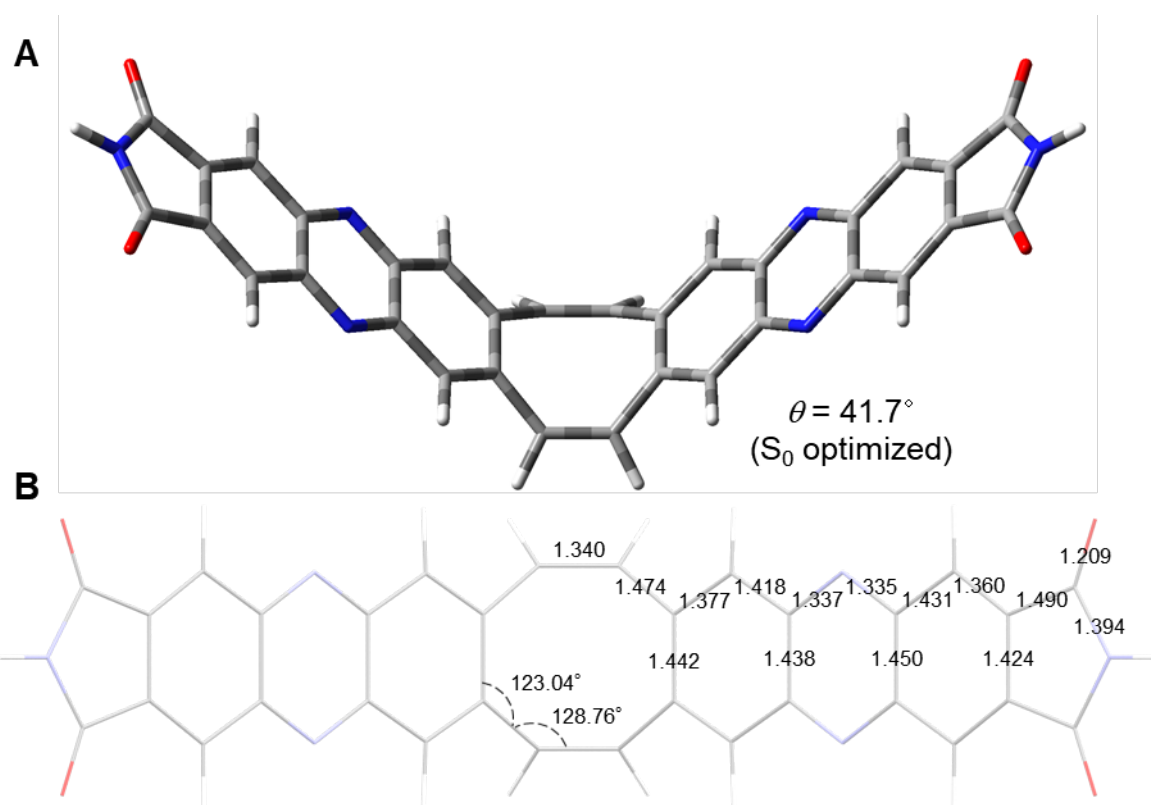
Figure S6.9. (**A**) S_0 optimized geometry of **FLAP1′** with bent C_{2v} symmetry (See Figure S6.17A). (**B**) Representative bond lengths (Å) and bond angles.

Figure S6.10. (**A**) S_1 optimized geometry of **FLAP1′** with planar D_{2h} symmetry that provides a B_{3g} state for the S_1 configuration (See Figure S6.17B). (**B**) Representative bond lengths (Å) and bond angles.

Figure S6.11. (A) S$_0$ optimized geometry of **FLAP2′** with bent C_{2v} symmetry (See Figure S6.18). **(B)** Representative bond lengths (Å) and bond angles.
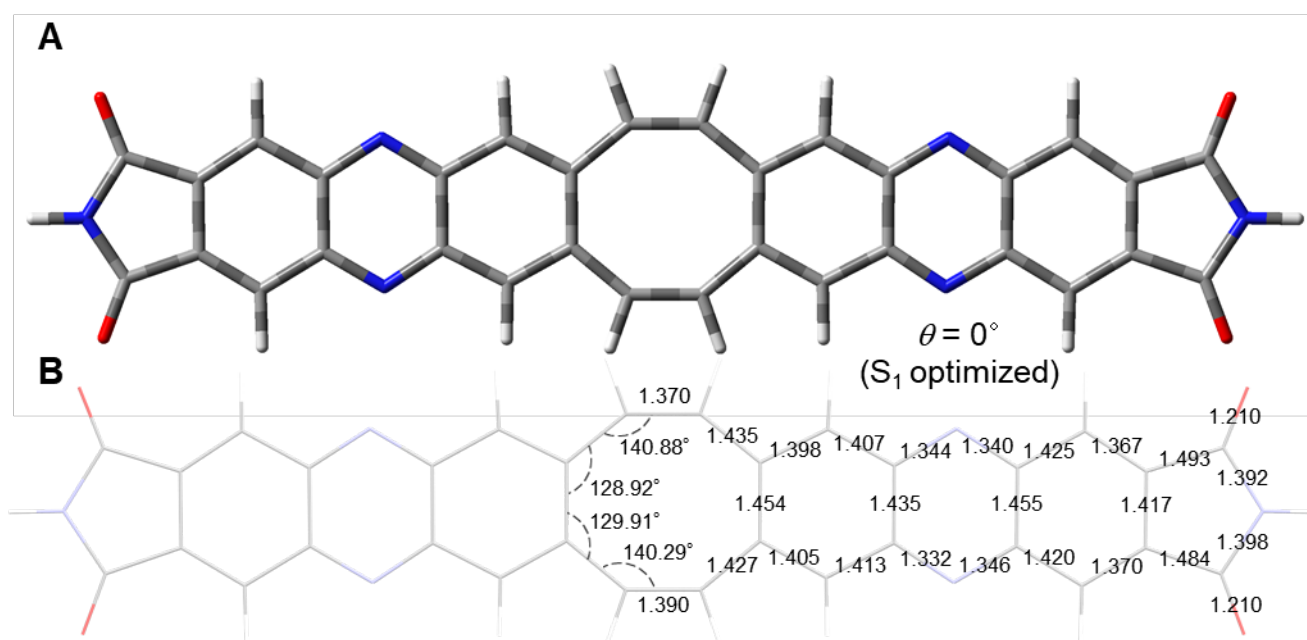

Figure S6.12. (A) S$_1$ optimized geometry of **FLAP2′** with planar C_{2v} symmetry that provides a B_2 state for the S$_1$ configuration (See Figure S6.4 and S6.19A). **(B)** Representative bond lengths (Å) and bond angles.
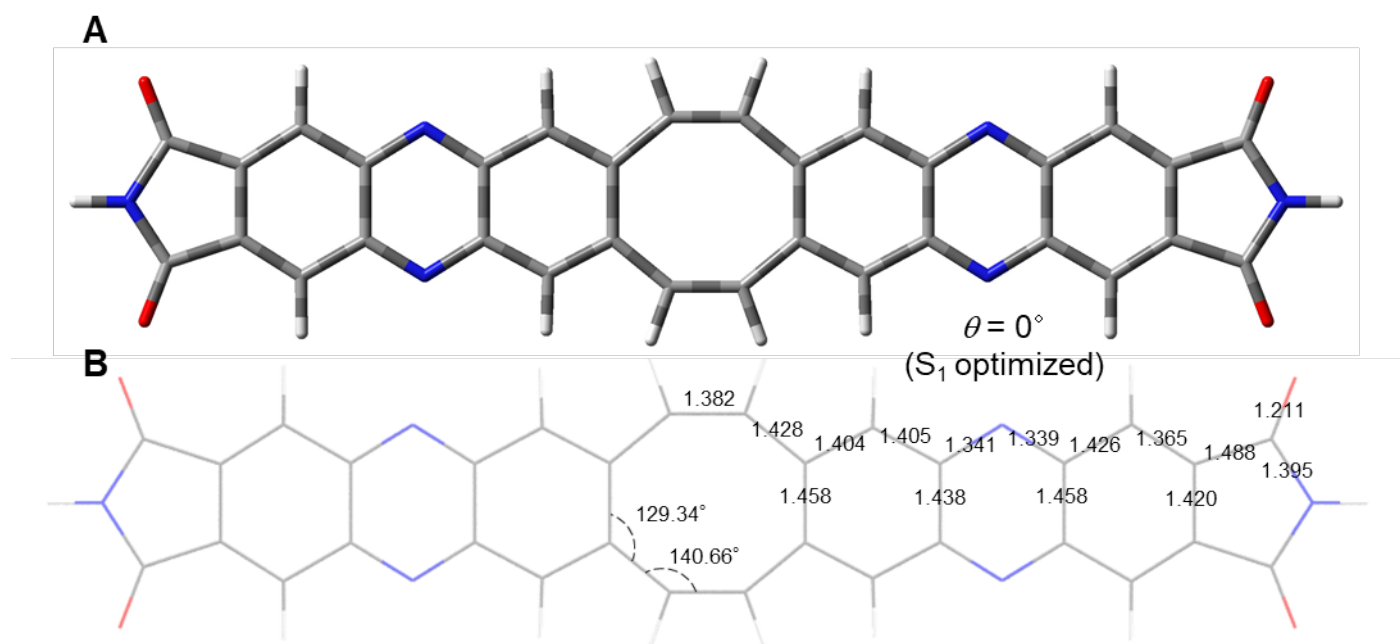
Figure S6.13. (A) S_1 optimized geometry of **FLAP2′** with planar D_{2h} symmetry that provides a B_{1u} state for the S_1 configuration (See Figure S6.4 and S6.19B). (B) Representative bond lengths (Å) and bond angles.
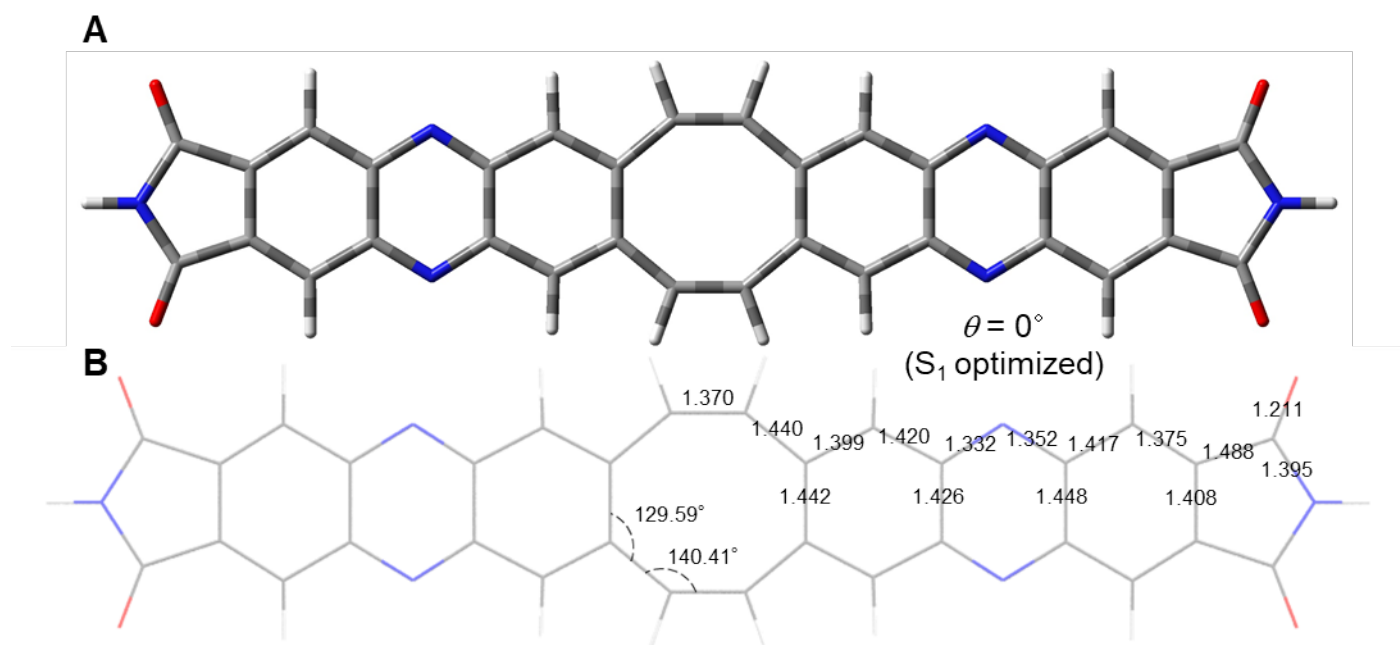

Figure S6.14. (A) S_1 optimized geometry of **FLAP2′** with planar D_{2h} symmetry that provides a B_{3g} state for the S_1 configuration (See Figure S6.4 and S6.19C). (B) Representative bond lengths (Å) and bond angles.

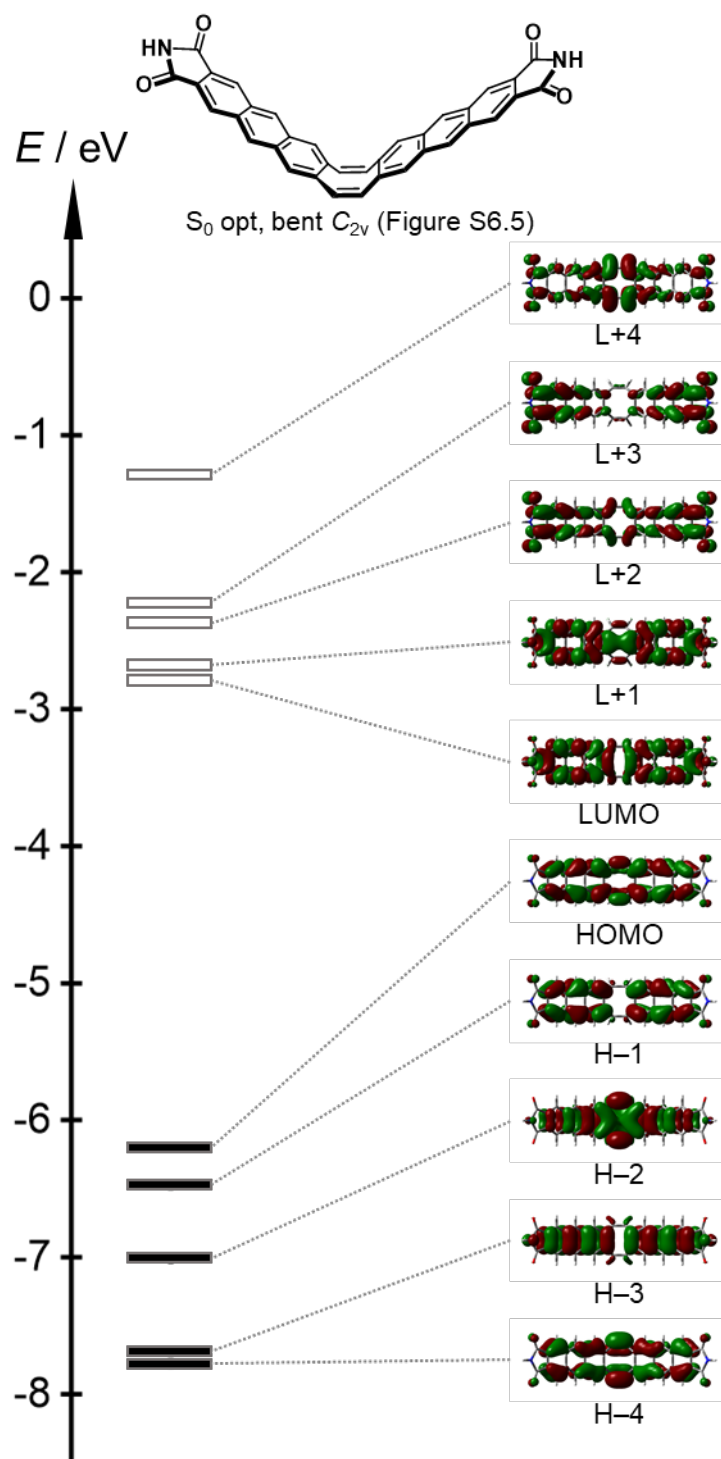## 6.3. Molecular orbitals of the S$_0$ and S$_1$ optimized geometries

Figure S6.15. Kohn-Sham molecular orbitals and their energy levels of **FLAP0′** at the S$_0$ geometry in Figure S6.5, optimized at the TD PBE0/6-31+G(d) level of theory.

Table S6.1. Excitation energy, configuration, and oscillator strength of the S$_0 \rightarrow$ S$_n$ (n $\leq$ 3) transitions for the S$_0$ optimized **FLAP0′** at the TD PBE0/6-31+G(d) level.

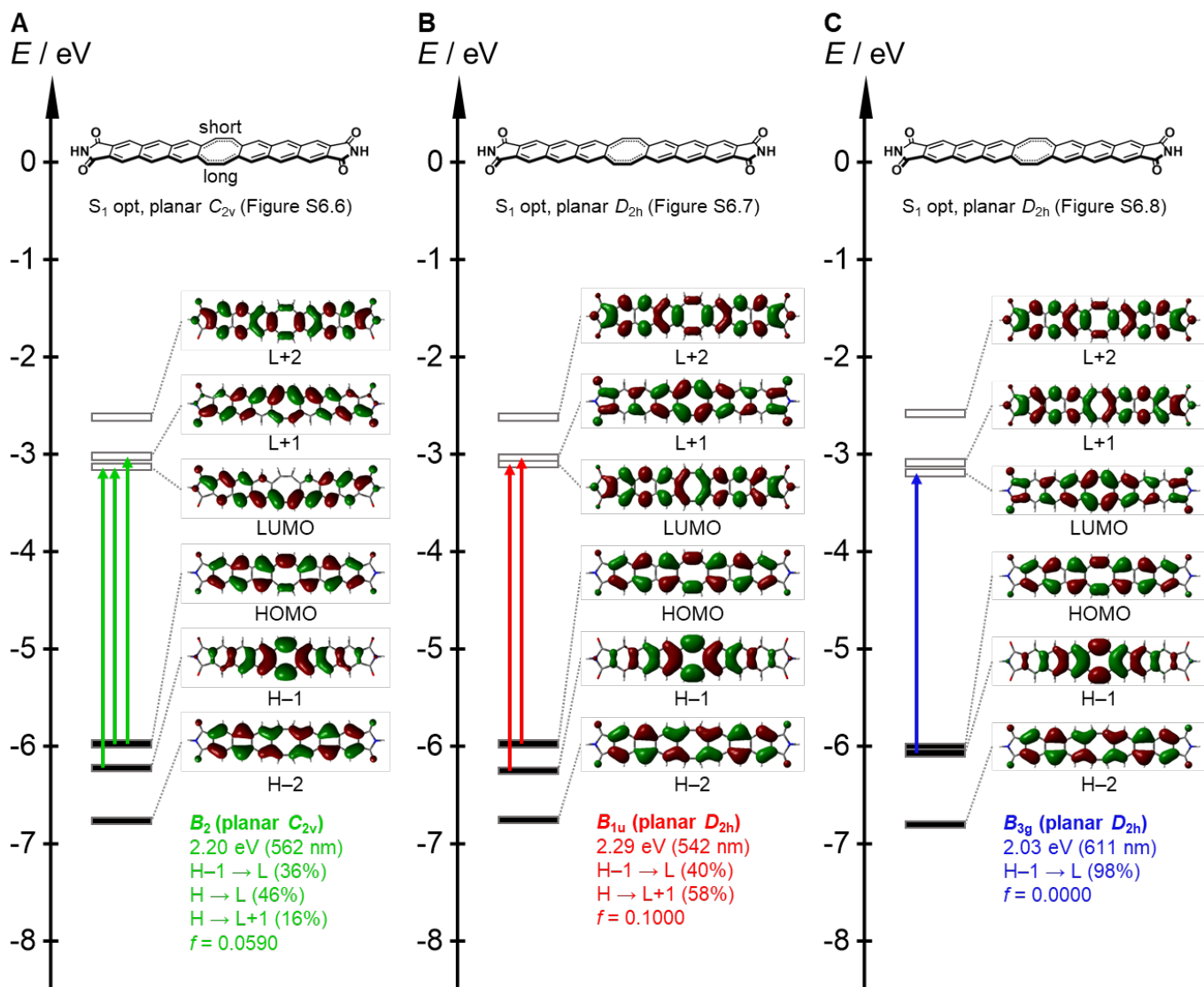| Transition	Excitation energy	Configuration	Oscillator strength
S$_0 \rightarrow$ S$_1$ (A_2)	2.89 eV (429 nm)	H $\rightarrow$ L (96%)	0.0000
S$_0 \rightarrow$ S$_2$ (B_1)	2.99 eV (414 nm)	H $\rightarrow$ L+1 (92%)	0.0382
S$_0 \rightarrow$ S$_3$ (B_2)	3.18 eV (389 nm)	H–2 $\rightarrow$ L (16%) H $\rightarrow$ L+2 (70%)	0.2441

Figure S6.16. Kohn-Sham molecular orbitals and their energy levels of **FLAP0′** at the different S_1 geometries in (**A**) Figure S6.6, (**B**) Figure S6.7, and (**C**) Figure S6.8, optimized at the TD PBE0/6-31+G(d) level of theory.
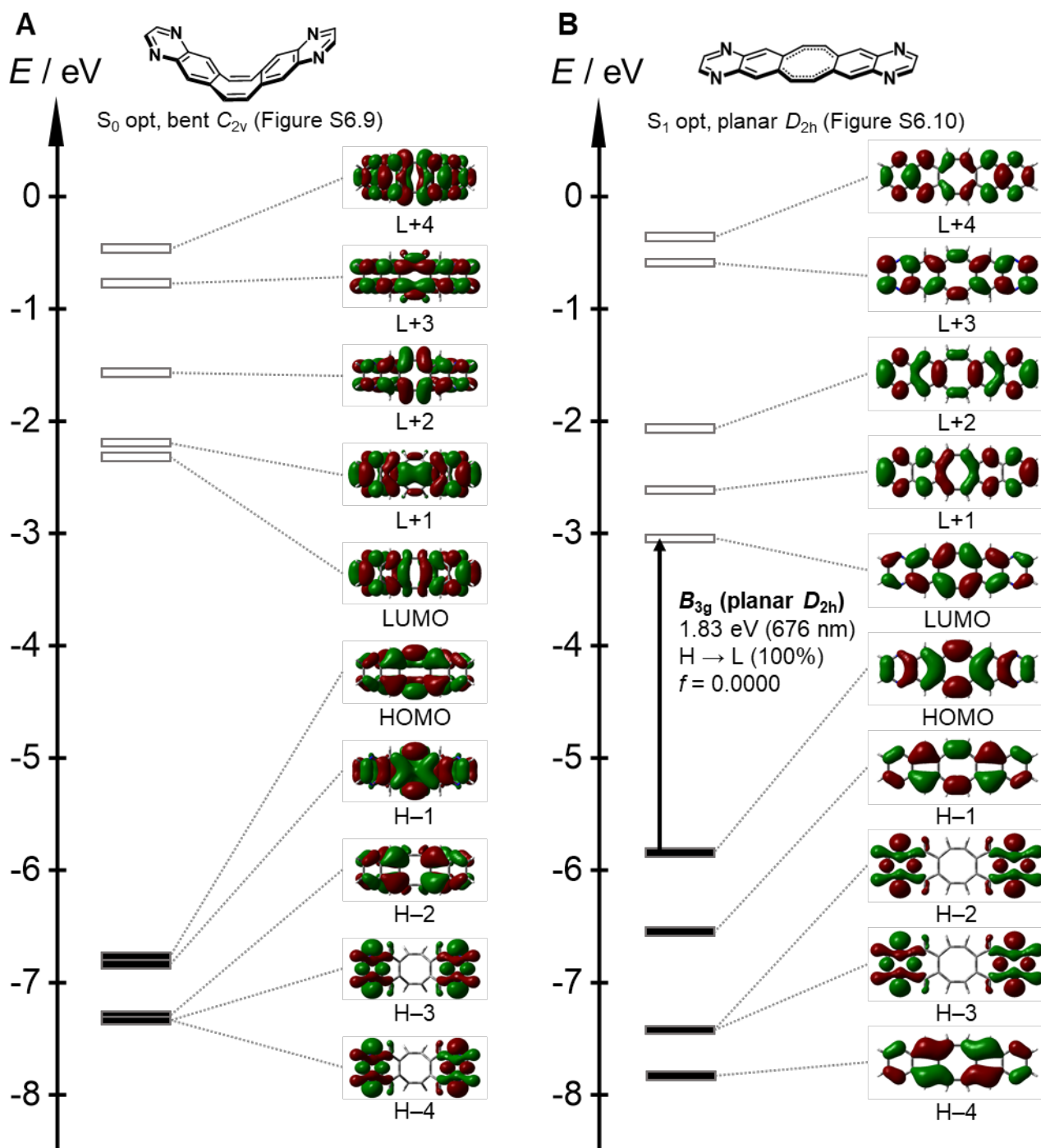
Figure S6.17. Kohn-Sham molecular orbitals and their energy levels of **FLAP1′** at (**A**) the S_0 geometry in Figure S6.9 and (**B**) at the S_1 geometry in Figure S6.10, optimized at the (TD) PBE0/6-31+G(d) level.

Table S6.2. Excitation energy, configuration, and oscillator strength of the $S_0 \rightarrow S_n$ ($n \leq 4$) transitions for the S_0 optimized **FLAP1′** at the TD PBE0/6-31+G(d) level.

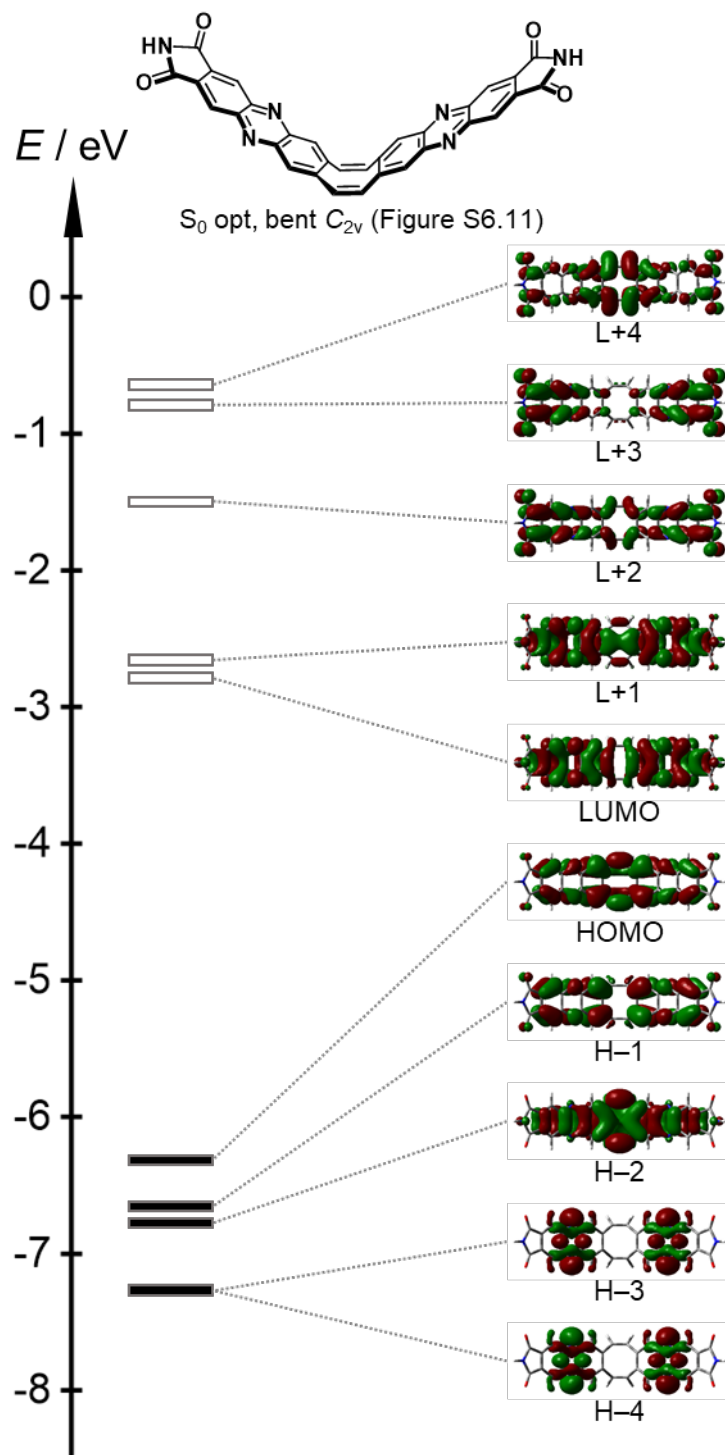| Transition	Excitation energy	Configuration	Oscillator strength
$S_0 \rightarrow S_1$ (B_2)	3.54 eV (350 nm)	H–4 → L+1 (44%) H–3 → L (53%)	0.0079
$S_0 \rightarrow S_2$ (A_1)	3.55 eV (350 nm)	H–4 → L (54%) H–3 → L+1 (44%)	0.0016
$S_0 \rightarrow S_3$ (A_2)	3.76 eV (330 nm)	H → L (95%)	0.0000
$S_0 \rightarrow S_4$ (B_2)	3.77 eV (329 nm)	H–1 → L (86%) H → L+2 (10%)	0.2182

S31

Figure S6.18. Kohn-Sham molecular orbitals and their energy levels of **FLAP2′** with different bent angles. The representative molecular orbitals and their energy levels were calculated at the TD PBE0/6-31+G(d) level.

Table S6.3. Excitation energy, configuration, and oscillator strength of the $S_0 \rightarrow S_n$ ($n \leq 5$) transitions for the S_0 optimized **FLAP2′** at the TD PBE0/6-31+G(d) level.

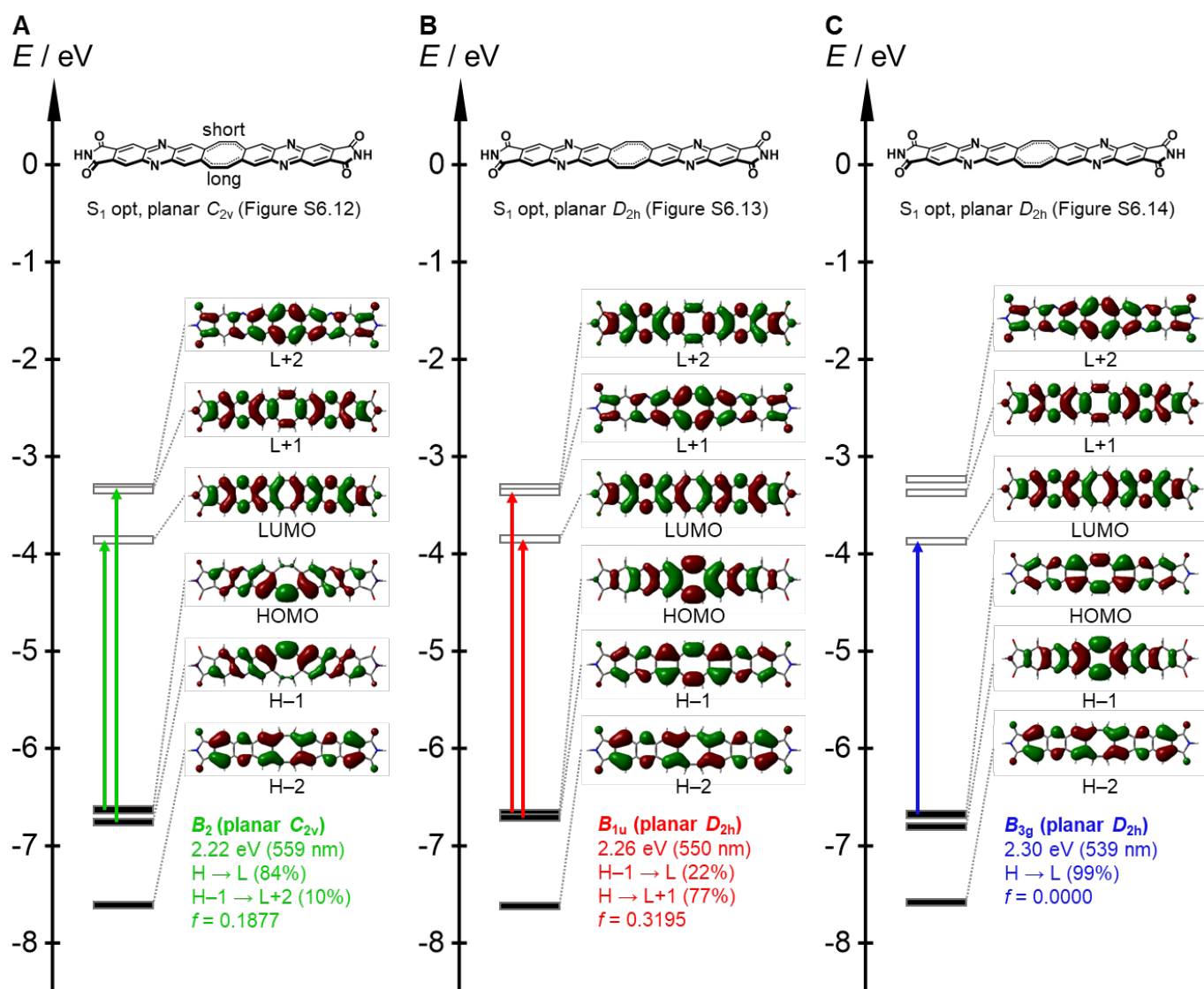| Transition	Excitation energy	Configuration	Oscillator strength
$S_0 \rightarrow S_1$ (A_2)	2.85 eV (435 nm)	H → L (96%)	0.0000
$S_0 \rightarrow S_2$ (B_1)	2.96 eV (419 nm)	H → L+1 (94%)	0.0204
$S_0 \rightarrow S_3$ (B_2)	3.04 eV (408 nm)	H–4 → L+1 (42%) H–3 → L (53%)	0.0215
$S_0 \rightarrow S_4$ (A_1)	3.04 eV (407 nm)	H–4 → L (55%) H–3 → L+1 (43%)	0.0002
$S_0 \rightarrow S_5$ (B_2)	3.19 eV (389 nm)	H–2 → L (83%)	0.4128

Figure S6.19. Kohn-Sham molecular orbitals and their energy levels of **FLAP2′** at the different S_1 geometries in (**A**) Figure S6.12, (**B**) Figure S6.13, and (**C**) Figure S6.14, optimized at the TD PBE0/6-31+G(d) level of theory.

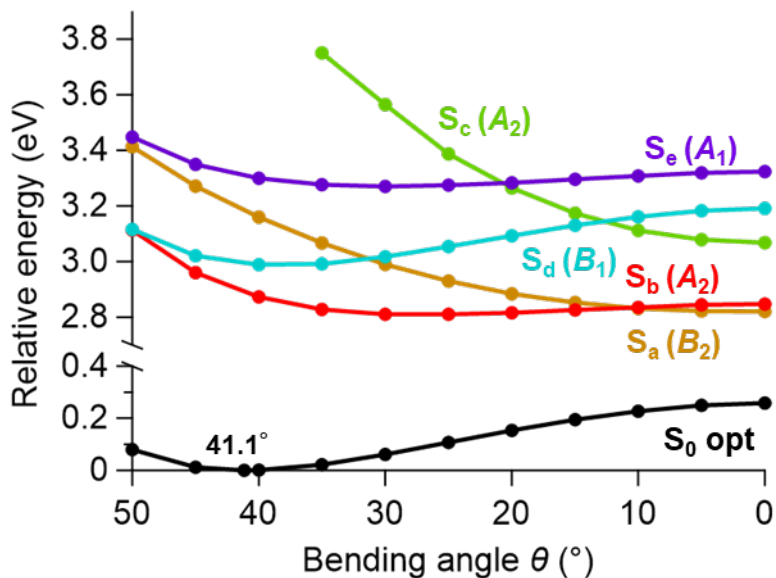## 6.4. Excited-state energy levels and molecular orbitals calculated for the S_0 optimized geometries

Figure S6.20. Potential energy diagram of the ground state S_0 and excited states S_a, S_b, S_c, S_d, and S_e for **FLAP0′** with fixed bent angles of COT. The molecular geometries are optimized in S_0.
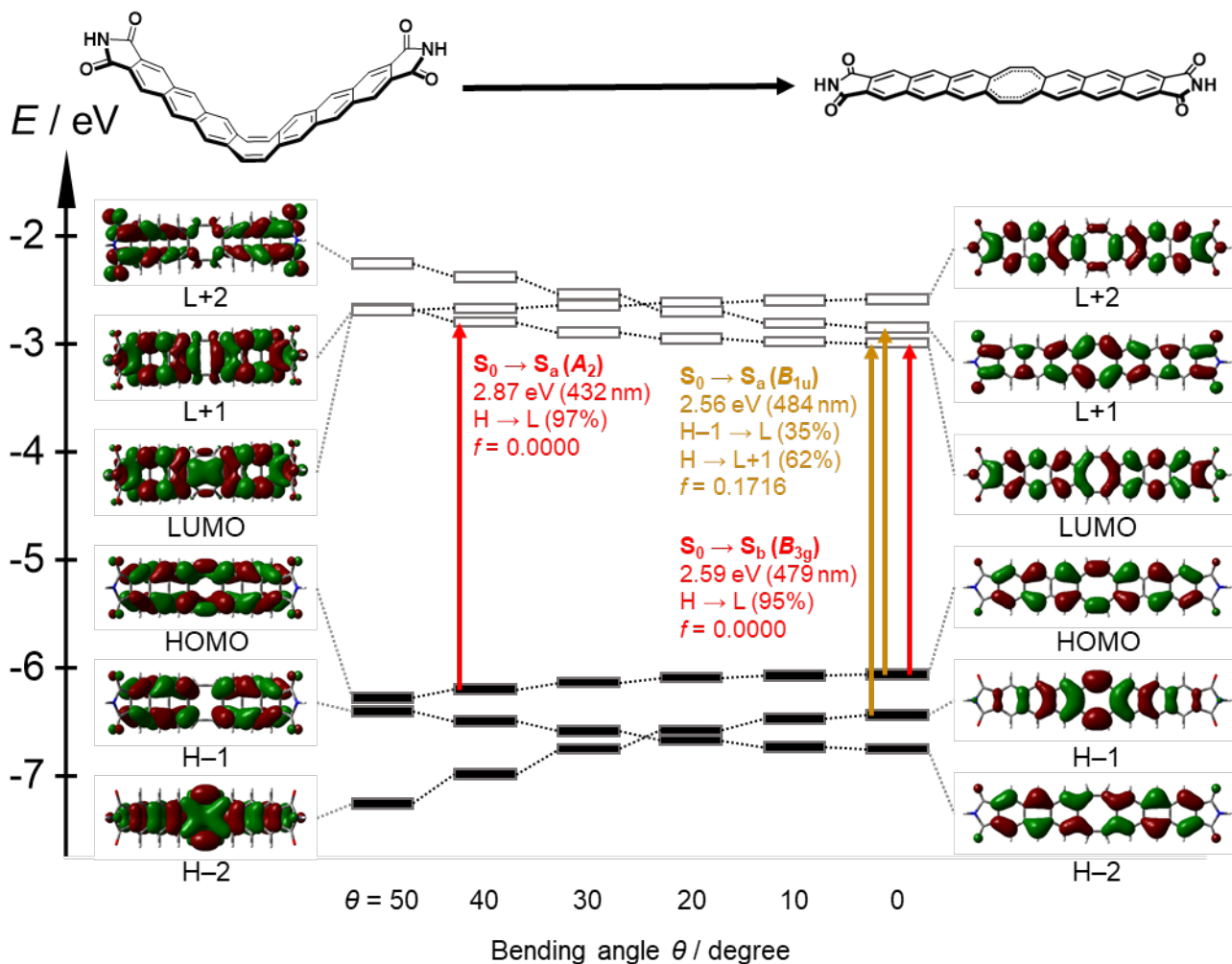

Figure S6.21. Kohn-Sham molecular orbitals and their energy levels of **FLAP0′** with different bent angles. DFT optimized geometries at the PBE0/6-31+G(d) level in S_0 were used for the TD-DFT calculations at the same level.
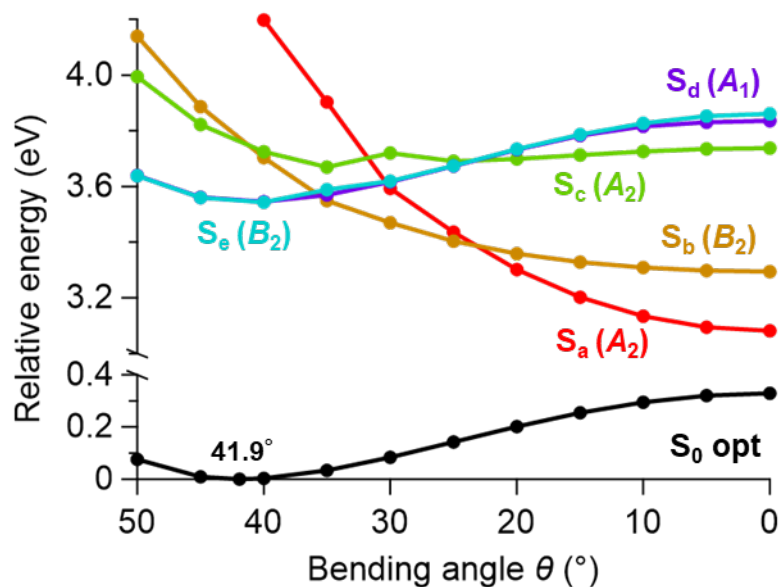
Figure S6.22. Potential energy diagram of the ground state S_0 and excited states S_a, S_b, S_c, S_d, and S_e for **FLAP1′** with fixed bent angles of COT. The molecular geometries are optimized in S_0.
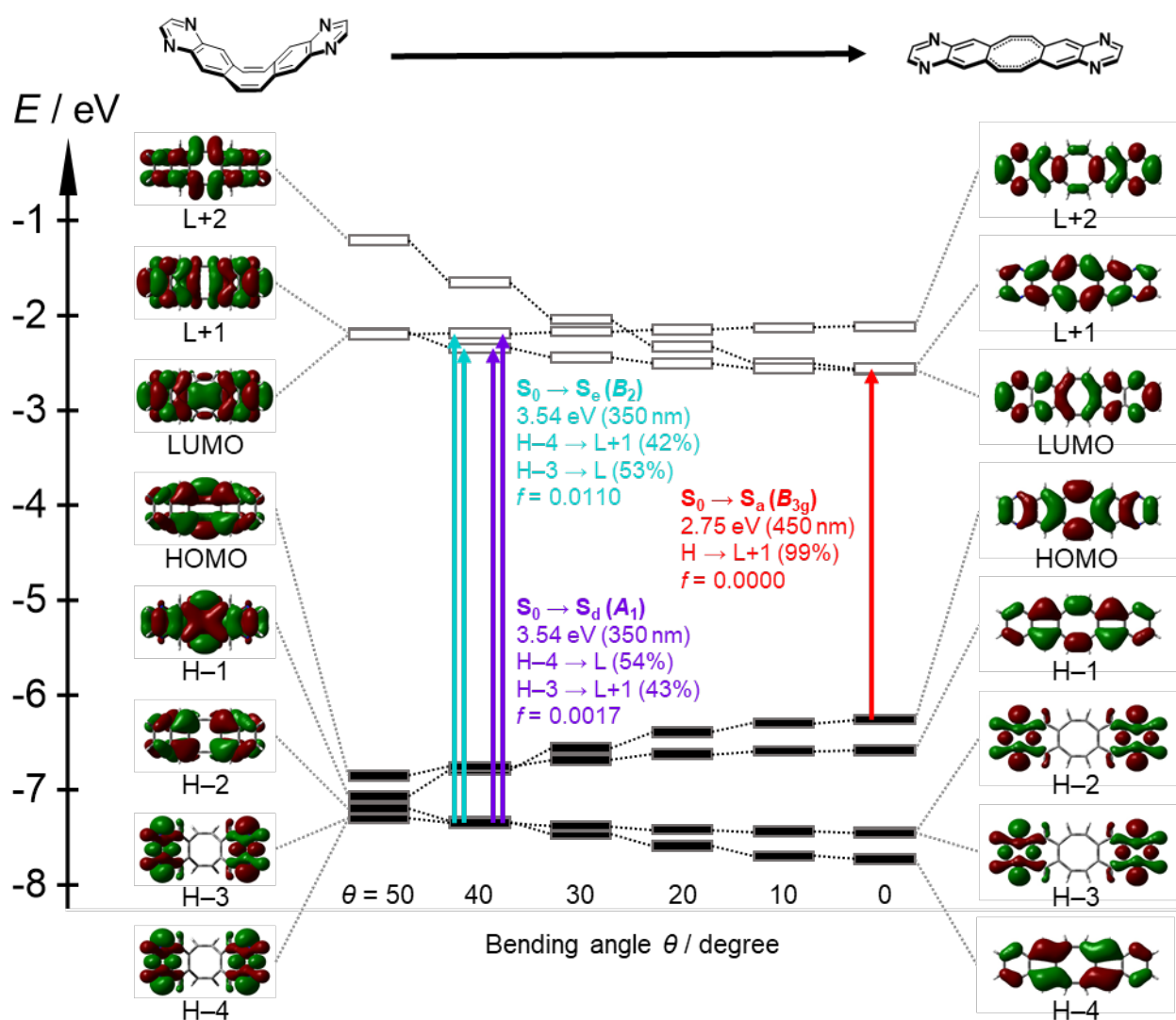

Figure S6.23. Kohn-Sham molecular orbitals and their energy levels of **FLAP1′** with different bent angles. DFT optimized geometries at the PBE0/6-31+G(d) level in S_0 were used for the TD-DFT calculations at the same level.

Figure S6.24. Potential energy diagram of the ground state S_0 and excited states S_a, S_b, S_c, S_d, and S_e for **FLAP2′** with fixed bent angles of COT. The molecular geometries are optimized in S_0.

Figure S6.25. Kohn-Sham molecular orbitals and their energy levels of **FLAP2′** with different bent angles. DFT optimized geometries at the PBE0/6-31+G(d) level in S_0 were used for the TD-DFT calculations at the same level.
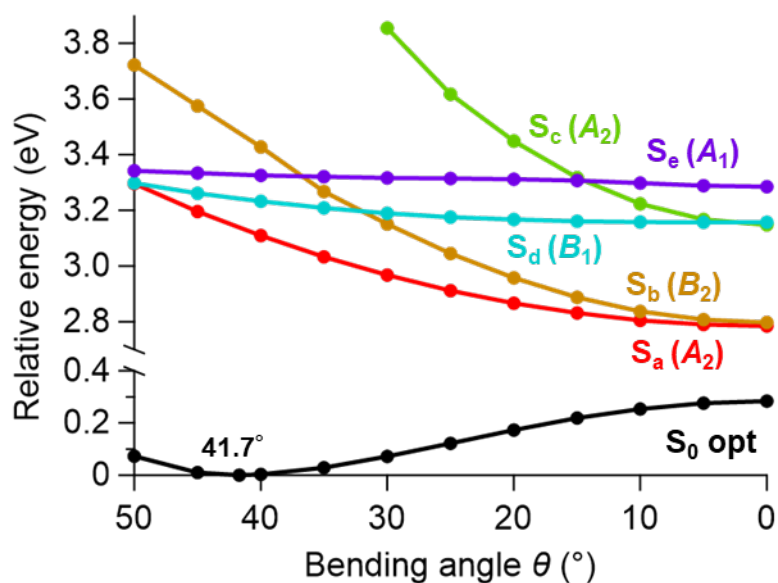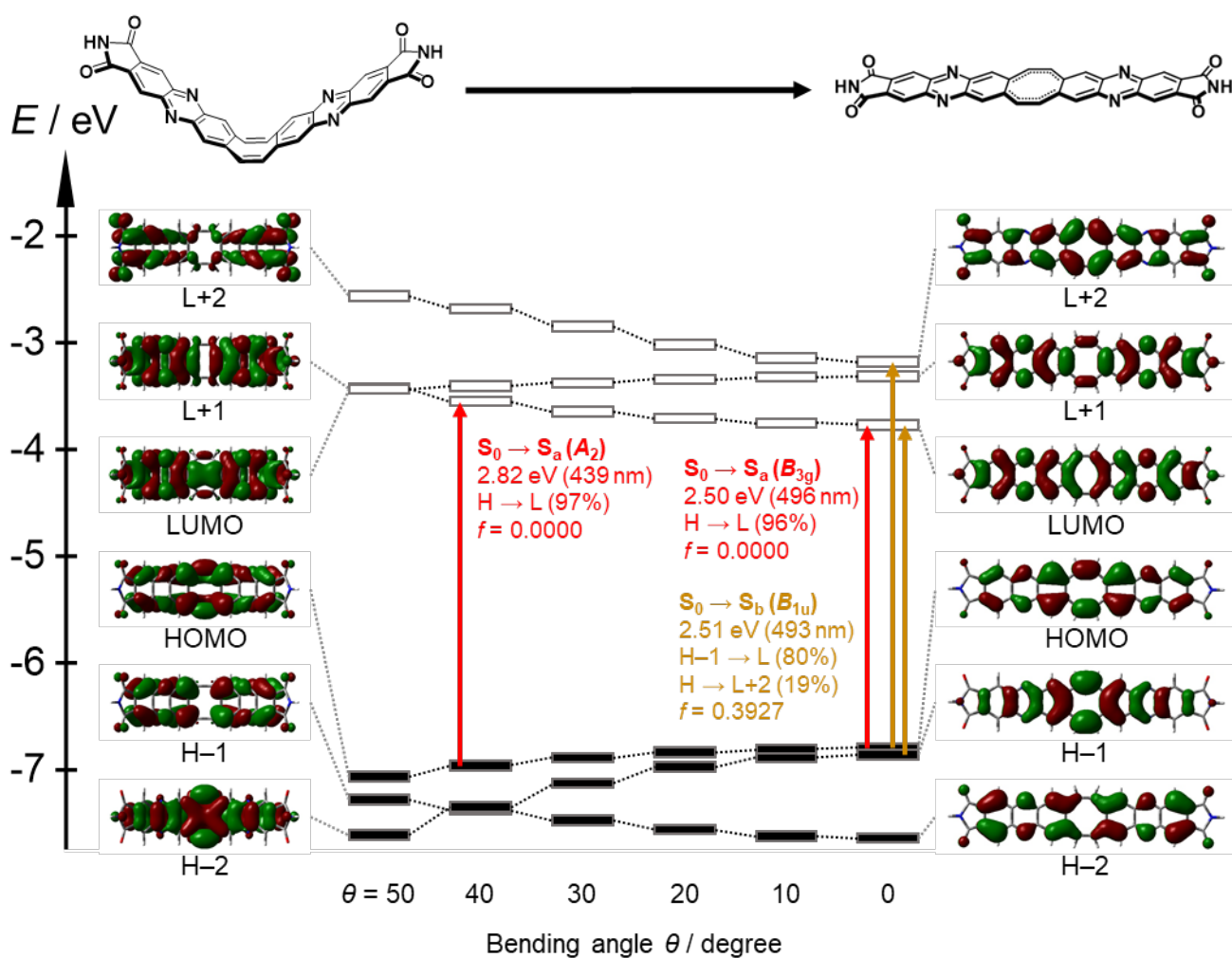
7. Supporting references

[S1]   R. Kimura, H. Kuramochi, P. Liu, T. Yamakado, A. Osuka, T. Tahara, S. Saito, *Angew. Chem. Int. Ed.* **2020**, *59*, 16430–16435.

[S2]   D. Kuzuhara, W. Furukawa, N. Aratani, H. Yamada, *J. Porphyrins Phthalocyanines* **2020**, *24,* 489–497.

[S3]   R. Kotani, H. Sotome, H. Okajima, S. Yokoyama, Y. Nakaike, A. Kashiwagi, C. Mori, Y. Nakada, S. Yamaguchi, A. Osuka, A. Sakamoto, H. Miyasaka, S. Saito, *J. Mater. Chem. C* **2017**, *5*, 5248.

[S4]   G. M. Sheldrick, *Acta Crystallogr.* **2015**, *A71*, 3–8.

[S5]   G. M. Sheldrick, *Acta Crystallogr.* **2015**, *C71*, 3–8.

[S6]   T. Förster, G. Hoffmann, *Z. Phys. Chem.* **1971**, *75*, 63.

[S7]   R. Kotani, H. Sotome, H. Okajima, S. Yokoyama, Y. Nakaike, A. Kashiwagi, C. Mori, Y. Nakada, S. Yamaguchi, A. Osuka, A. Sakamoto, H. Miyasaka, S. Saito, *J. Mater. Chem. C* **2017**, *5*, 5248.

[S8]   Gaussian 16, Revision A.03, M. J. Frisch, G. W. Trucks, H. B. Schlegel, G. E. Scuseria, M. A. Robb, J. R. Cheeseman, G. Scalmani, V. Barone, G. A. Petersson, H. Nakatsuji, X. Li, M. Caricato, A. V. Marenich, J. Bloino, B. G. Janesko, R. Gomperts, B. Mennucci, H. P. Hratchian, J. V. Ortiz, A. F. Izmaylov, J. L. Sonnenberg, D. Williams-Young, F. Ding, F. Lipparini, F. Egidi, J. Goings, B. Peng, A. Petrone, T. Henderson, D. Ranasinghe, V. G. Zakrzewski, J. Gao, N. Rega, G. Zheng, W. Liang, M. Hada, M. Ehara, K. Toyota, R. Fukuda, J. Hasegawa, M. Ishida, T. Nakajima, Y. Honda, O. Kitao, H. Nakai, T. Vreven, K. Throssell, J. A. Montgomery, Jr., J. E. Peralta, F. Ogliaro, M. J. Bearpark, J. J. Heyd, E. N. Brothers, K. N. Kudin, V. N. Staroverov, T. A. Keith, R. Kobayashi, J. Normand, K. Raghavachari, A. P. Rendell, J. C. Burant, S. S. Iyengar, J. Tomasi, M. Cossi, J. M. Millam, M. Klene, C. Adamo, R. Cammi, J. W. Ochterski, R. L. Martin, K. Morokuma, O. Farkas, J. B. Foresman, and D. J. Fox, Gaussian, Inc., Wallingford CT, 2016.